

Supporting Information

For

Can One Determine the Density of an Individual Synthetic Macromolecule?

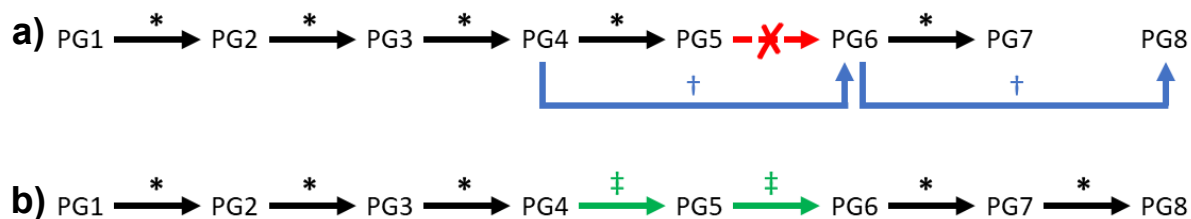
Daniel Messmer^{a)*}, Antoni Sánchez-Ferrer^{b)}, Sebastian Tacke^{c)}, Hao Yu^{a)}, Harald Nüsse^{d)}, Jürgen Klingauf^{d)}, Roger Wepf^{d)}, Martin Kröger^{a)}, Avraham Halperin^{e)†}, Raffaele Mezzenga^{b)*}, A. Dieter Schlüter^{a)*}

- a) Department of Materials, ETH Zürich, Polymer Chemistry & Polymer Physics, Vladimir-Prelog-Weg 5, 8093 Zürich, Switzerland (current address of H. Yu: Laboratory of Packaging Engineering, School of Printing and Packaging, Wuhan University, 430000 Wuhan, People's Republic of China)
 - b) Department of Health Sciences and Technology, ETH Zürich, Laboratory of Food and Soft Materials, Schmelzbergstrasse 9, 8092 Zürich, Switzerland
 - c) Scientific Center for Optical and Electron Microscopy, ETH Zürich, Otto-Stern-Weg 3, 8093 Zürich, Switzerland (current address of S. Tacke: MPI for Molecular Physiology, Structural Biochemistry, Otto-Hahn-Strasse 1, 44227 Dortmund, Germany; current address of R. Wepf: Centre for Microscopy and Microanalysis, University of Queensland, St. Lucia, Queensland 4072, Australia)
 - e) Institute of Medial Physics and Biophysics, Westfälische Wilhelms-Universität Münster, Robert-Koch-Strasse 31, 48149 Münster, Germany
 - f) Laboratoire de Spectrometrie Physique, CNRS University Joseph Fourier, BP 87, 38402 Saint Martin d'Hères cedex, France
- † Avraham Halperin unfortunately passed away during the work leading to this manuscript.

Contents

Can one determine the density of an individual synthetic macromolecule?	1
Contents	2
1. Polymer Samples.....	3
1.1. Series A.....	3
1.2. Series B.....	3
1.3. Comparison of Series A and Series B; Comments regarding structural perfection and MPL values 3	
1.4. Details concerning the preparation of compact DP pills.....	5
2. Detailed Methods to Derive Density Values	7
2.1. ρ_{bulk} from hydrostatic weighing	7
2.2. ρ_{bulk} from density gradient column measurements.....	8
2.3. ρ_{SAXS} from unit cell geometry	10
2.4. $\rho_{\text{SEM/TEM}}$ from individual-molecule dimensions.....	13
2.5. ρ_{qSTEM} from STEM-based mass mapping	16
3. Density Values Obtained for Series B.....	24
4. Discussion of Potential Sources of Error in the Determination of Density Values.....	27
4.1. MPL values for the derivation of ρ_{SAXS} and $\rho_{\text{SEM/TEM}}$	28
4.2. Chain cross-section models for the derivation of ρ_{SAXS} , $\rho_{\text{SEM/TEM}}$ and ρ_{qSTEM}	31
4.3. Sources of error & uncertainty for ρ_{bulk}	33
4.4. Sources of error & uncertainty for ρ_{SAXS}	33
4.5. Sources of error & uncertainty for $\rho_{\text{SEM/TEM}}$	33
4.6. Sources of error & uncertainty for ρ_{qSTEM}	34
5. Additional SAXS and WAXS results	34
6. Bibliography	37

1. Polymer Samples



Scheme S 1: Representations of the routes resulting in the DPs of a) series A and b) series B. Each arrow corresponds to a two-step sequence (deprotection and dendronization); * standard “ $g + 1$ ” dendronization protocol;¹ † “ $g + 2$ ” dendronization protocol;^{2,3} ‡ modified “ $g + 1$ ” dendronization protocols.⁴

1.1. Series A

The polymers from Series A (PG1 – PG8) were prepared as discussed previously (Scheme S 1a).^{1,2} Briefly, their preparation started from PG1 and employed a “ $g + 1$ ” dendronization protocol up to PG5. The preparation of PG6 using the same protocol failed due to main-chain scission;^{5,6} A “ $g + 2$ ” dendronization protocol starting from PG4 was used in the preparation of PG6 in order to avoid this issue.³ PG7 and PG8 were prepared from PG6 by application of the “ $g + 1$ ” and “ $g + 2$ ” protocols, respectively.²

1.2. Series B

Recent improvements of synthetic methodology have given access to PG1 – PG8 in a series of all-homologous DPs, *i.e.* each DP except PG1 was prepared from the corresponding ($g - 1$) precursor *via* a “ $g + 1$ ” dendronization step. As indicated in Scheme S 1b, this necessitated modification of the standard protocols.⁴ Namely, this involved the use of Alloc instead of Boc terminal *N*-protecting groups for PG5. This necessitated the use of correspondingly modified $g = 1$ dendronization agent and different methods for deprotection. For the preparation of PG7 and PG8, the standard, NHBoc-based “ $g + 1$ ” protocol was employed again, as the respective precursors proved stable to NHBoc deprotection.^{4,6}

1.3. Comparison of Series A and Series B; Comments regarding structural perfection and MPL values

The “ $g + 2$ ” steps leading to PG6 and PG8 involved the use of a $g = 2$ dendronization agent⁷ which is substantially larger ($M = 1266.4$ Da, Figure S 1b) than the normally employed $g = 1$ dendronization reagent ($M = 565.1$ Da; Figure S 1a). As the steric bulk of the former reagent is consequently greater, the dendronization reactions leading from PG4 to PG6 and from PG6 to PG8 proceed with significantly lower functional group conversion values than steps utilizing the “ $g + 1$ ” dendronization protocol. Consequently, the DPs in series A of $g > 5$ (see Table S 1) are structurally more deficient than their

analogues from series B (see Table S 2). The functional group conversion X after each dendronization step was determined for both series using a well-established defect labelling method employing 2,4-dinitrofluorobenzene (Sanger's reagent, see Figure S 1c).^{1,2,4,8,9}

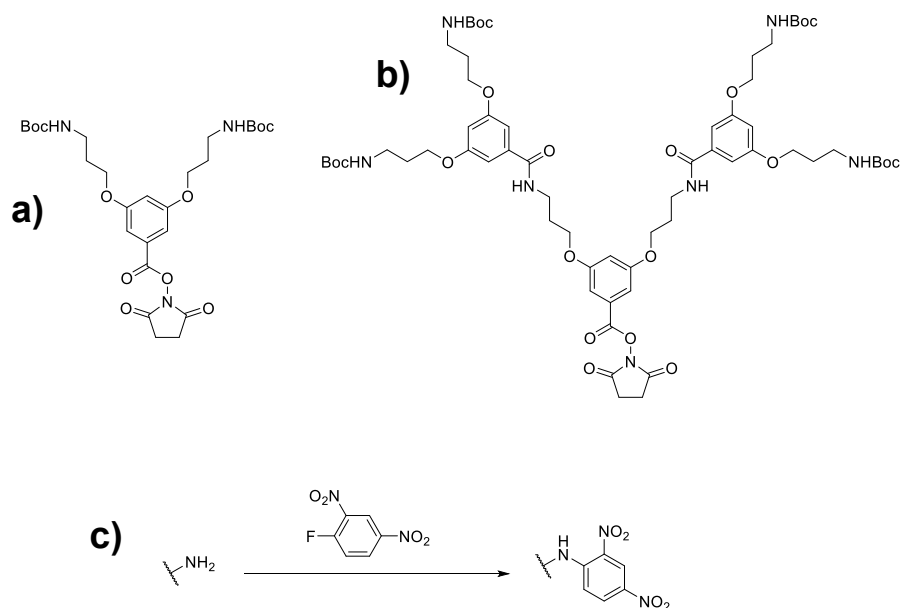


Figure S 1: Chemical structures of the a) 1st and b) 2nd generation dendronization reagents; c) labelling of an unreacted, primary amine with Sanger's reagent (dendron structure omitted for clarity); the resulting dinitroaniline derivative is yellow-colored ($\epsilon_{360} = 16400 \text{ M}^{-1}\text{cm}^{-1}$).⁸

However, this defect labeling method relies on sufficient solubilization of unreacted, terminal amino groups. For DPs of $g > 6$, this is not guaranteed anymore – the defect labeling results indicate higher molar masses than are possible in view of g_{max} considerations (see main text, Fig. 1b).^{4,10} Therefore, the lower of the two values $\langle M_g \rangle$ (the average molar mass per repeating unit calculated from defect labelling) and M_g^{max} (the theoretically achievable molar mass per repeating unit in a DP; see Table S 1 & Table S 2), termed M_{exp} , is used when an externally sourced MPL value is called for, as is the case for the use of the corresponding value M_{label} in the calculations of $\rho_{\text{SEM/TEM}}$ and ρ_{SAXS} (see below).

We must point out that a certain circularity cannot be avoided in this context: Density calculations depend on g_{max} , which depends on the minimum extension of the dendritic matter packed densely around the DP backbone. This in turn is a function of an assumed density value (Table S 1 & Table S 2: $\rho = 1.4 \text{ g cm}^{-3}$).

Table S 1: Sanger labelling data and corresponding calculations for series A.⁴ a) Functional group conversion X calculated from results of defect labeling. b) Molar mass of one ideal, isolated DP repeating unit; c) average molar mass per repeating unit obtained from defect labeling; d) maximum theoretically possible molar mass per DP repeating unit assuming $\rho = 1.4 \text{ g cm}^{-3}$; e) assuming $L_{\text{RU}} = 0.252 \text{ nm}$.

Polymer	Route	X [%] ^{a)}	M_g^{ideal} [g mol ⁻¹] ^{b)}	$\langle M_g \rangle$ [g mol ⁻¹] ^{c)}	M_g^{max} [g mol ⁻¹] ^{d)}	M_{exp} [g mol ⁻¹]	M_{label} [g mol ⁻¹ nm ⁻¹] ^{e)}
PG2	«g + 1»	99.85	1223.5	1220.8	1223.5	1220.8	4844.4
PG3	«g + 1»	99.9	2625.1	2617.2	2625.1	2617.2	10386
PG4	«g + 1»	99.81	5428.5	5401.5	5428.4	5401.5	21435
PG5	«g + 1»	99.78	11035	10952	11035	10952	43460
PG6	«g + 2»	91.29	22248	20016	22248	20016	79429
PG7	«g + 1»	99.79	44675	40492	43342	40492	160683
PG8	«g + 2»	97.26	89528	78896	55325	55325	219544

Table S 2: Sanger labelling data and corresponding calculations for series B.⁴ a) Functional group conversion X calculated from results of defect labeling. b) Molar mass of one ideal, isolated DP repeating unit; c) average molar mass per repeating unit obtained from defect labeling; d) maximum theoretically possible molar mass per DP repeating unit assuming $\rho = 1.4 \text{ g cm}^{-3}$; e) assuming $L_{\text{RU}} = 0.252 \text{ nm}$.

Polymer	Route	X [%] ^{a)}	M_g^{ideal} [g mol ⁻¹] ^{b)}	$\langle M_g \rangle$ [g mol ⁻¹] ^{c)}	M_g^{max} [g mol ⁻¹] ^{d)}	M_{exp} [g mol ⁻¹]	M_{label} [g mol ⁻¹ nm ⁻¹] ^{e)}
PG2	«g + 1»	99.93	1223.5	1221.9	1223.5	1221.9	4848.8
PG3	«g + 1»	99.86	2625.1	2618.0	2625.1	2618.0	10389
PG4	«g + 1»	99.76	5428.4	5393.7	5428.4	5393.7	21404
PG5 (Alloc)	«g + 1» (modified)	99.69	10522	10433	10522	10433	41401
PG6	«g + 1» (modified)	99.62	22248	21969	22248	21969	86095
PG7	«g + 1»	99.77	44674	44030	43342	43342	17199
PG8	«g + 1»	99.67	89527	87937	55325	55325	219544

1.4. Details concerning the preparation of compact DP pills

Samples used for hydrostatic weighing as well as for density gradient column and SAXS measurements were prepared by vacuum hot-pressing of loose, freeze-dried DP powders (see main text, Fig. 2a) as obtained from DP synthesis. To that end, the apparatus displayed in Figure S 2 was employed, consisting essentially of a cylindrical stainless steel mould inside a brass vacuum flask.

For pill preparation, the brass flask was pre-heated between the plates of a temperature-controlled hot-press (Rondol) set to 80 °C (PG1), 90 °C (PG2) or 100 – 105 °C (PG3 – PG8), *i.e.* significantly above T_g of the DPs.¹¹ Meanwhile, the mould was set into its nylon holder together with the base plate and the bore was filled with the appropriate amount of DP (~10 – 30 mg). The interior assembly was completed, inserted into the pre-heated vacuum flask and left to thermally equilibrate for 1 min between the plates of the press without applying significant force. The entire assembly was then slowly and carefully evacuated to $p \leq 0.1$ mbar using an external vacuum pump (Vacuubrand RC5), and then a clamping force of 0.1 – 0.5 kN was applied for 3 min. Clamping was released and the assembly was cooled to RT using the press' active water cooling. The glassy, brittle DP pills (see main text, Fig. 2a) were then carefully removed from the mould. All parts in contact with DP were cleaned and rinsed with methylene chloride before re-use.

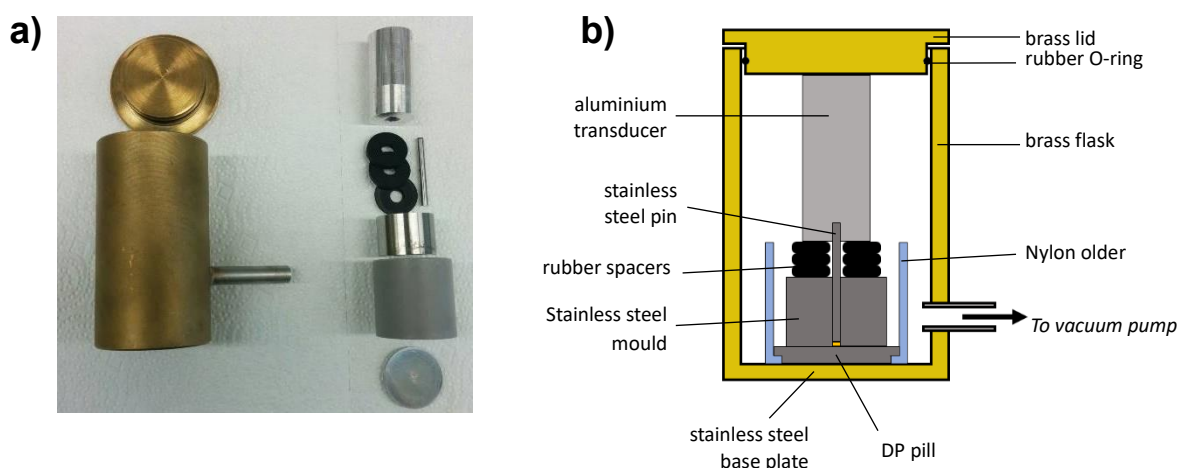


Figure S 2: a) Photograph of the disassembled apparatus and b) schematic representation of the assembled apparatus used for vacuum hot-press moulding of DPs.

2. Detailed Methods to Derive Density Values

2.1. ρ_{bulk} from hydrostatic weighing

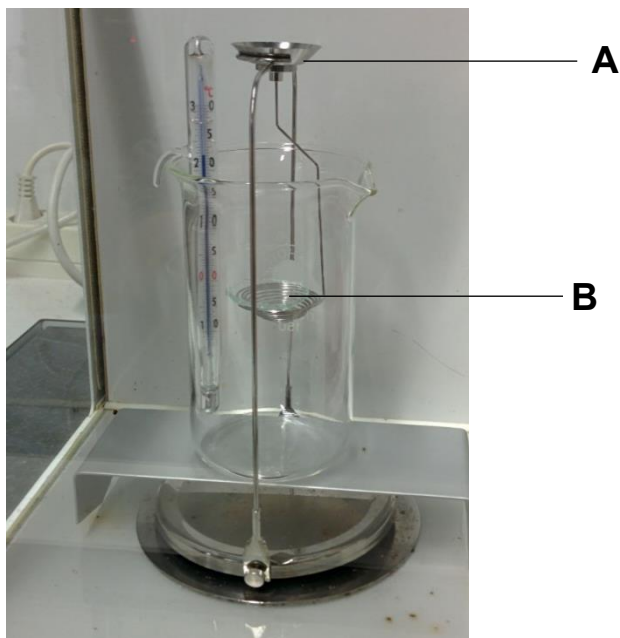


Figure S 3: Photograph of the density measurement kit assembled on the analytical balance. A section of a watchglass was set into the wire basket to prevent the small DP samples from slipping between the wires.

For density measurements using the classical Archimedean method of hydrostatic weighing, the density of the working fluid hexane (ρ_{hex} ; bottle left to stand in the room overnight before measurements to assure thermal equilibrium) was first determined for each run of measurements. This was necessary as room temperature varied slightly ($\sim 22\text{-}24\text{ }^{\circ}\text{C}$). For each DP pill, five separate density measurements were conducted, each consisting of first weighing the sample in the pan on top of the kit (Figure S 3, A) to afford w_{air} , taring the balance, and then determining its buoyant force when submerged in hexane (w_{hex}) on the wire basket (Figure S 3, B). The density can then be determined using Eq. S 1. The density values shown in Fig. 3a in the main text correspond to the averages of five measurements for each pill, and the values reported in Tab. 1 correspond to the average densities obtained for the individual pills (usually three pills per DP sample).

$$\rho_{\text{bulk}} = -\rho_{\text{hex}} \frac{w_{\text{air}}}{w_{\text{hex}}}$$

Eq. S 1

Hexane was selected as the working fluid over water due to its lower surface tension, thereby reducing issues with the immersion of the small samples. Denser organic liquids were not used due to concerns of possible swelling; DPs are at least partially soluble in most solvents ranging from polar protic and aprotic solvents (MeOH, DMF, DMSO) all the way to fairly apolar liquids such as toluene. Longer-chain, slightly denser alkanes such as decane were not used due to their higher boiling points, which complicate the drying of samples between measurements.

2.2. ρ_{bulk} from density gradient column measurements

For the measurement of density by the gradient column method, a simple in-house built set-up was used, consisting of a standard chromatography column (inner diameter: 3 cm, length: 50 cm), a rigid aluminium frame with a heavy steel base plate, and a digital linear encoder (Figure S 4a). For density measurements, DP samples (compact pills, see section 1.4) and hollow glass sphere density standards (8 standards linearly covering the range $\rho = 1.002 - 1.4009 \text{ g cm}^{-3}$, H&W Fitzgerald) were lowered to the bottom of the column by means of a titanium wire basket attached to a nylon string. The density gradient was then established from the bottom of the column by slow vacuum aspiration (850 mbar) of the working fluid, which was provided from a vigorously stirred flask. The flask initially contained deionized water and was connected to a reservoir containing a saturated aqueous solution of sodium bromide (Figure S 4b), which was aspirated continuously as vacuum was applied to the column. To avoid bubble formation, both liquids were degassed thoroughly by vigorous stirring at 80 mbar for 3 min directly before use in the gradient column. Before reading out density values, the column was left to equilibrate for at least 12 h while sitting undisturbed at a fairly constant room temperature of 23 – 23.5 °C. The density gradient was discarded when visible bubbles had formed on column walls, standards, samples, or if samples and standards stuck together. Only the positions of individual samples and standards clearly separated from the column walls were considered.

Positions $h(\rho)$ (centers of the pills and calibration spheres) were measured using the digital linear encoder attached to the frame in parallel to the column. To avoid parallax errors, a metal fork surrounding the column was attached to the measurement piece, providing a read-out error of ± 0.3 mm (repeatability). From the measured positions $h(\rho)$ of the hollow glass sphere standards, a first-order exponential calibration curve (Figure S 4c, Eq. S 2, with fit parameters h_0 , A_1 and t_1) was produced which served as a gauge for the density of samples according to the measured position (see Figure S 4c for an example). Accordingly, the density ρ of an individual DP pill was determined using Eq. S 3. The values shown in the main text (Tab. 1) correspond to the average of three individual pills measured per DP sample.

$$h(\rho) = h_0 + A_1 e^{\rho/t_1}$$

Eq. S 2

$$\rho(h) = t_1 \ln \frac{h - h_0}{A_1}$$

Eq. S 3

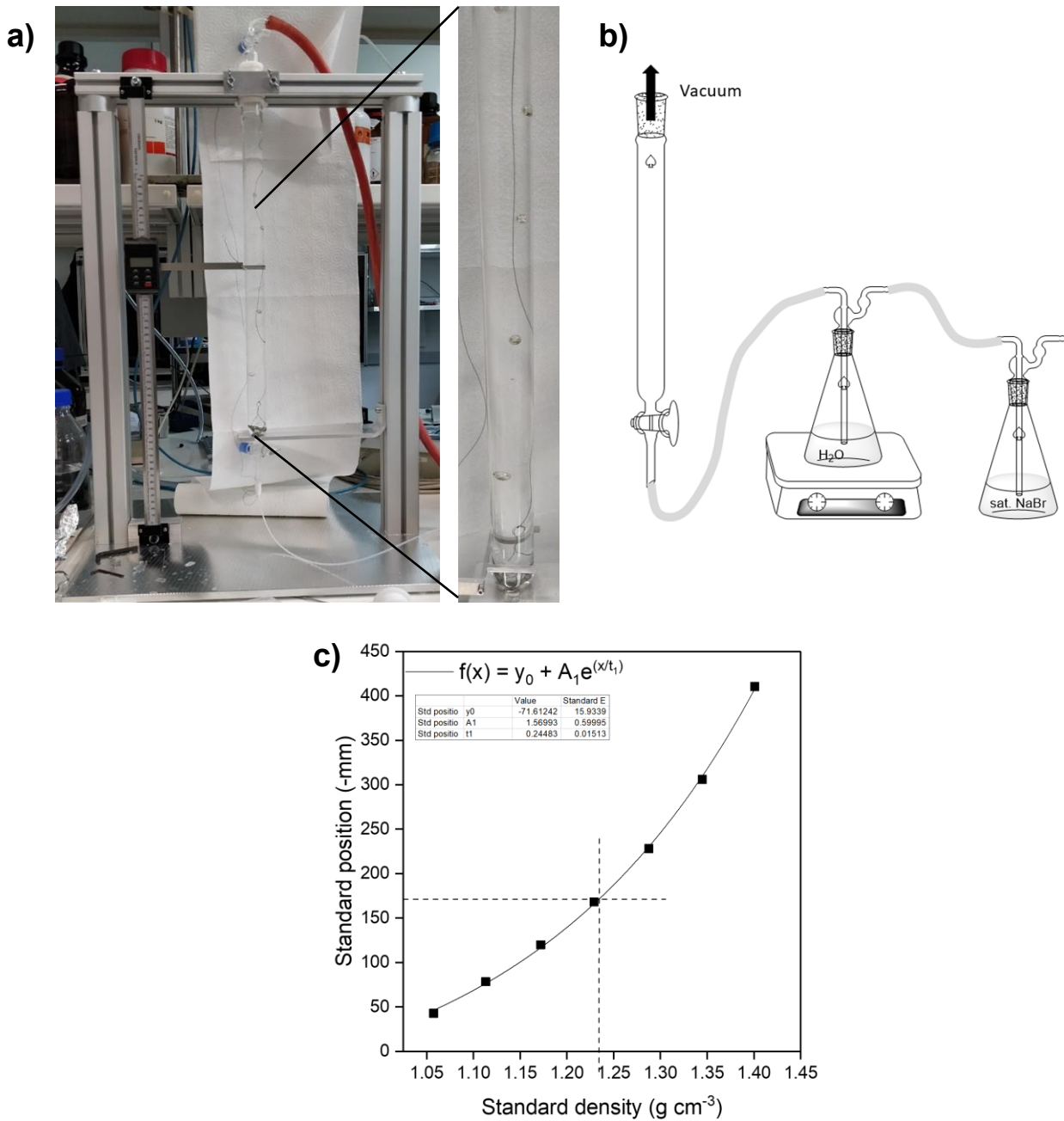


Figure S 4: a) Photograph of the in-house built density gradient column setup, the inset showing the filled column including standards; b) schematic representation of the apparatus used to establish the density gradient; c) example of a gradient calibration curve (fit to Eq. S 2), with sample position and density marked by dashed lines.

2.3. ρ_{SAXS} from unit cell geometry

As shown in Figure S 5, the density values obtained from SAXS results depend strongly on the fit geometry. Table S 3 and Figure S 5 contain the planar unit cell parameters and density values derived for rhombohedral fit geometry displayed in Fig. 3b (main text), in addition to data for tetragonal, hexagonal and oblique geometries. Figure S 6 shows the individual SAXS curves for PG1 – PG8 (compare Fig. 3b in the main text) and the corresponding fits for columnar rhombohedral packing.

Table S 3: Planar unit cell parameters obtained for columnar oblique, tetragonal, hexagonal and rhombohedral SAXS peak fits and corresponding values of ρ_{SAXS} for DPs from series A (see main text, Fig. 3b). a) Samples of $g = 1, 2$ show insufficient numbers of peak for accurate unit cell fitting.

g	Oblique (no constraints)				Tetragonal ($a = b, \gamma = 90^\circ$)		Hexagonal ($a = b, \gamma = 60^\circ$)		Rhombohedral ($a = b$)		
	a (nm)	b (nm)	γ ($^\circ$)	ρ_{SAXS} (g cm^{-3})	a (nm)	ρ_{SAXS} (g cm^{-3})	a (nm)	ρ_{SAXS} (g cm^{-3})	a (nm)	γ ($^\circ$)	ρ_{SAXS} (g cm^{-3})
1 ^{a)}	2.46	2.46	60	0.66	2.13	0.76	2.46	0.66	2.46	60	0.66
2 ^{a)}	3.53	3.53	60	0.74	3.06	0.86	3.53	0.74	3.53	60	0.74
3	6.45	3.67	38	1.17	4.01	1.07	4.63	0.93	4.78	57	0.90
4	8.29	4.62	40	1.43	5.38	1.23	6.21	1.06	6.81	52	0.97
5	10.36	5.66	45	1.75	7.28	1.36	8.41	1.18	9.89	47	1.00
6	10.31	5.48	52	2.98	8.08	2.02	9.33	1.75	12.63	40	1.29
7	9.99	5.50	56	5.85	8.28	3.89	9.56	3.37	10.85	50	2.97
8	10.99	5.90	57	6.64	9.26	4.22	10.70	3.66	13.67	43	2.86

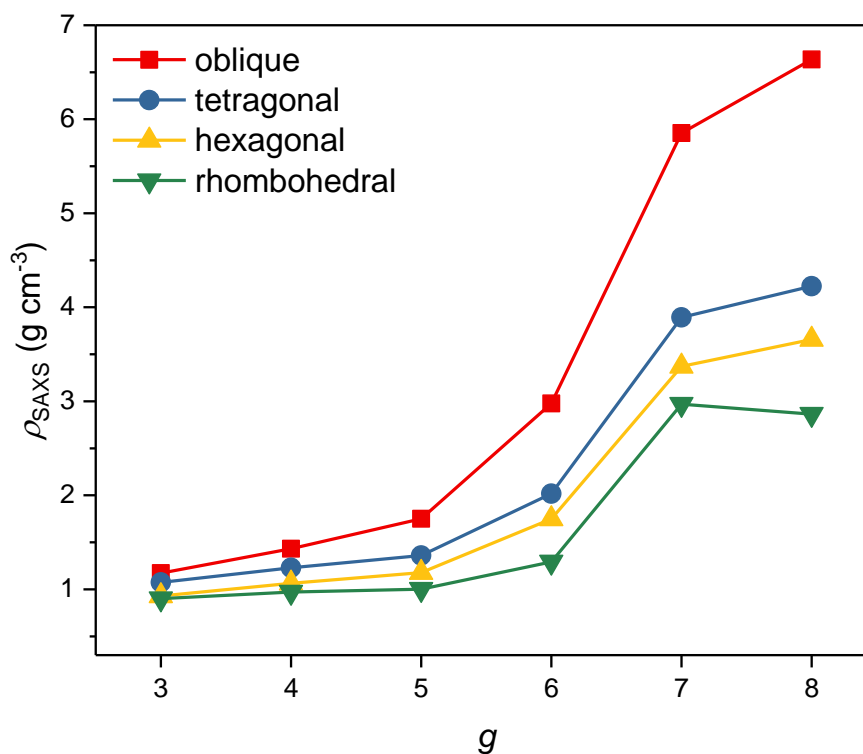


Figure S 5: ρ_{SAXS} values from different fit geometries as noted in Table S 3.

SAXS intensity profile curves were deconvoluted by using Lorentzian fit curves in order to identify the exact peak maxima positions q , corresponding to the diffraction planes of a columnar phase. Each peak maximum is related to a plane distance d via the relationship

$$d = \frac{2\pi}{q}$$

Eq. S 4

Columnar phases are 2D Bravais lattices, and the first three peaks correspond to the family of planes for which the scattering wave vectors q_{hk} and the Miller indices (hk) are q_{10} , q_{01} and q_{11} , and (10), (01) and (11), respectively. In order to calculate the cell unit parameters (a , b and γ), Eq. S 5 was used:

$$\frac{1}{d_{hk}^2} = \frac{1}{\sin^2 \gamma} \left(\frac{h^2}{a^2} + \frac{k^2}{b^2} - \frac{2hk \cos \gamma}{ab} \right)$$

Eq. S 5

By imposing the d -value for each peak, and solving the resulting system of three non-linear equations, the three unit cell parameters are obtained. Depending on the assumed Bravais lattice, extra restrictions may need to be imposed: For columnar oblique phase, all parameters are free, for the tetragonal phase $\gamma = 90^\circ$, for hexagonal phase $a = b$ and $\gamma = 60^\circ$, and for rhombohedral phase $a = b$. In order to check the goodness of the fit, the rest of the scattering peaks values were compared to the theoretical values when imposing the calculated lattice parameters.

To calculate density values ρ_{SAXS} from the unit cell parameters, one requires a suitable mass-per-length (MPL) value and it is necessary to calculate the cross-sectional area of a DP chain within the given packing geometry. The density values given in Table S 3 assume M_{label} values derived from M_{exp} (Table S 1; see section 4 of this SI for discussion). As the DP samples were carefully annealed, the DP chains in the bulk samples are likely strongly interdigitated, or else squished together. It is therefore reasonable to assume that the cross-section area of the DP chain within the self-assembled domains probed by SAXS corresponds to the unit cell area A_{cell} (Eq. S 6), permitting the calculation of ρ_{SAXS} using Eq. S 7.

$$A_{cell} = a \cdot b \cdot \sin \gamma$$

Eq. S 6

$$\rho_{SAXS} = \frac{M_{exp}}{L_{RU} A_{cell}} = \frac{M_{exp}}{V_{cell}} = \frac{M_{label}}{A_{cell}}$$

Eq. S 7

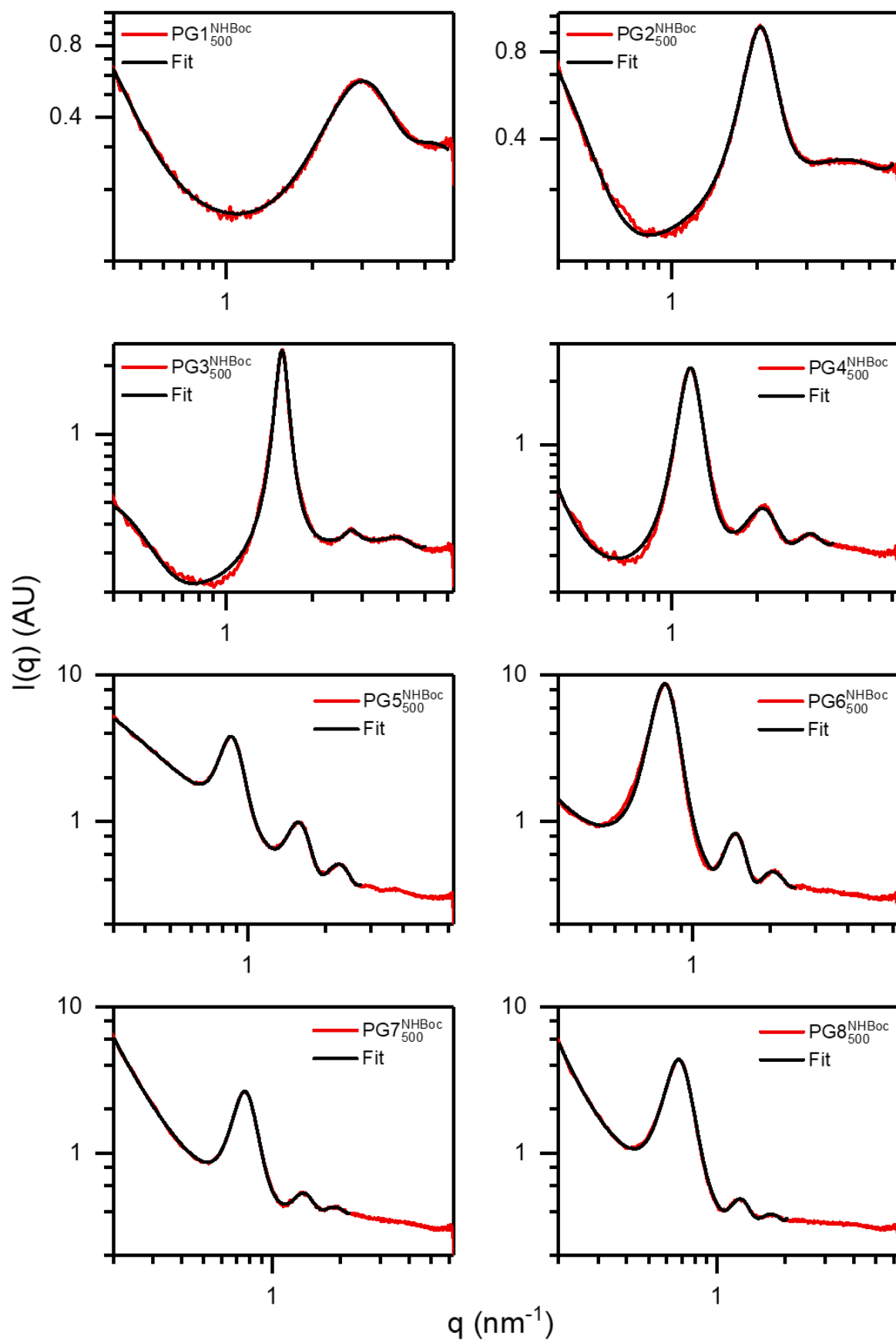


Figure S 6: SAXS curves for DPs of series A (compare Fig. 2b, main text) including the corresponding fit curves based on columnar rhombohedral packing.

2.4. $\rho_{SEM/TEM}$ from individual-molecule dimensions

The two shadowing methods described in the Methods and Materials section of the main text permit for the determination of the height and width of DPs, in the present case adsorbed on mica. Other flat substrates may fulfill the same purpose, as demonstrated in the previous publication from which data for PG1 – PG5 was taken, where mica, amorphous carbon and HOPG were used as substrates.¹⁰

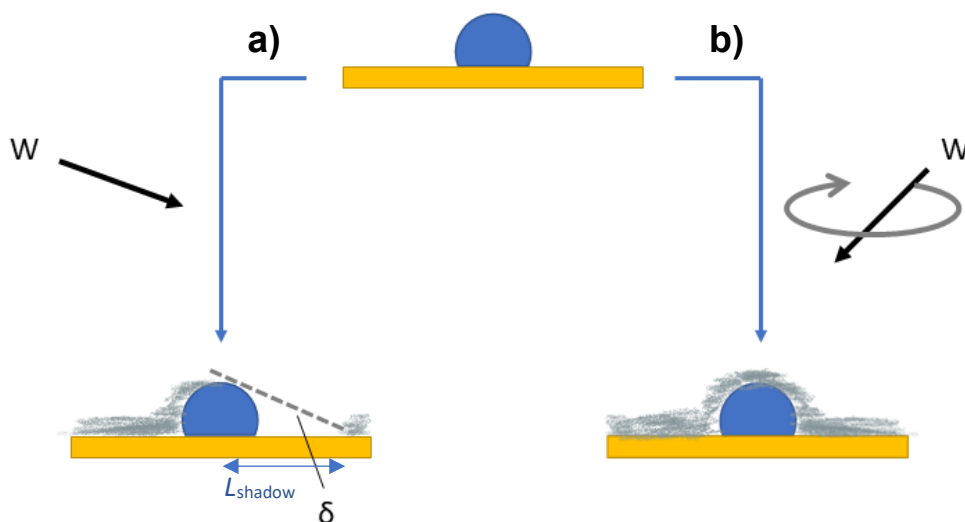


Figure S 7: Illustrations of the two tungsten coating procedures; a) unidirectional W-shadowing at an elevation angle $\delta = 7^\circ$ used to obtain h_{TEM} and b) rotary W-shadowing (from $\delta = 45^\circ$) used to obtain w_{SEM} .

The height h_{TEM} at a location along the DP backbone was determined from the length of the uncoated “shadow” L_{shadow} cast by the DP chain after unidirectional W-coating from an elevation angle of $\delta = 7^\circ$ relative to the sample plane (Figure S 7a; also see Fig. 2c in the main text and Figure S 9), using Eq. S 8.

$$h_{TEM} = L_{shadow} \tan \delta$$

Eq. S 8

The width w_{SEM} was measured directly in SEM images of rotary W-shadowed samples (Figure S 7b; also see Fig. 2d in the main text and Figure S 9), subtracting 0.7 nm to account for the thickness of the deposited tungsten layer.^{10,12} For both h_{TEM} and w_{SEM} , ~ 10 locations along several individual shadowed DPs were evaluated per DP generation (Figure S 9). The values listed in Table S 4 correspond to the averages of these measurements. It should be noted that while for $g = 2 - 5$ the relative standard deviations of h_{TEM} and w_{SEM} decrease continuously (absolute errors remain roughly constant), they start increasing again for $g > 5$. This observation is consistent with studies by AFM, which demonstrated increasing corrugation for PG6 – PG8 in series A.² This was at the time ascribed to large defects (see section 1.3). A similar trend is present in AFM images of the structurally more perfect DPs from series B however, suggesting that a shape transition away from a straight cylinder might take place due to proximity to g_{max} .⁴

Similar to the derivation of ρ_{SAXS} (see section 2.2), to calculate $\rho_{SEM/TEM}$ from h_{TEM} and w_{SEM} one requires both an MPL value and a cross-section model. The former are identical to those used for the calculation of ρ_{SAXS} (M_{label} as listed in Table S 1). The two metal shadowing techniques provide the

extreme cross-sectional extensions of the deposited DP chains, but they do not provide the cross-section geometry. DPs are very compact, and while they flatten out to some degree when adsorbed to surfaces (see Table S 4), they do not spread substantially, unlike *e.g.* bottle-brush polymers.¹³ Hence, the assumption of a cut-circular cross-section as displayed in Figure S 8a appears reasonable and is indeed supported by MD simulations of DPs deposited on mica.¹⁴ The area A_{CC} of the cut circle is given by Eq. S 9, corresponding to the area of a circle of radius w_{SEM} minus the circular segment defined by the angle β . The angle can be obtained from given values of w_{SEM} and h_{TEM} using Eq. S 10.

$$A_{CC} = \frac{\pi}{4} w_{SEM}^2 - \frac{1}{8} w_{SEM}^2 (\beta - \sin\beta)$$

Eq. S 9

$$\beta = 2\cos^{-1}\left(1 - \frac{2(w_{SEM} - h_{TEM})}{w_{SEM}}\right)$$

Eq. S 10

The density $\rho_{SEM/TEM}$ can then be calculated using Eq. S 11. The same approach can be used for other cross-section models (*e.g.* an approximately rectangular cross-section as indicated in Figure S 8b) by substituting A_{CC} for the corresponding cross-section area (the product of w_{SEM} and h_{TEM}) for rectangular cross-section.

$$\rho_{SEM/TEM} = \frac{M_{label}}{A_{CC}}$$

Eq. S 11

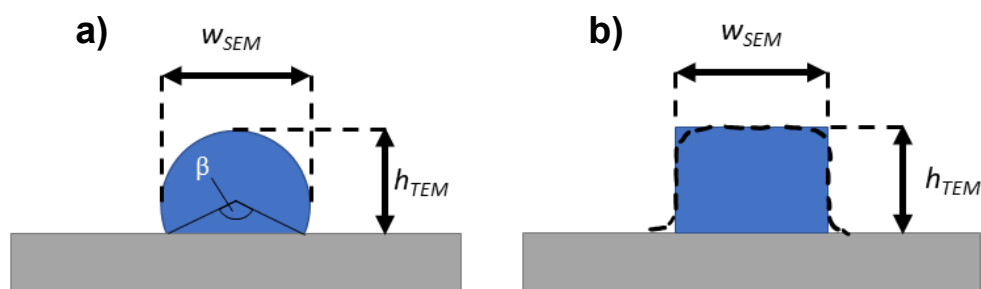


Figure S 8: Cross-section models for deposited DPs: a) cut circle (*i.e.* a circle missing a circular segment defined by the angle β); b) rectangular.

Table S 4: Values of h_{TEM} , w_{SEM} , the aspect ratio of h and w , and $\rho_{\text{SEM/TEM}}$ (assuming cut circular or rectangular cross-section). a) see previously published results.¹⁰

g	h_{TEM} (nm)	w_{SEM} (nm)	h/w	$\rho_{\text{SEM/TEM}}$ (g cm ⁻³)	
				cut circle	rectangular
2	$2.3 \pm 0.4^{\text{a}}$	$3.1 \pm 0.4^{\text{a}}$	0.74 ± 0.22	1.3 ± 0.4	1.3 ± 0.3
3	$3.4 \pm 0.5^{\text{a}}$	$4.5 \pm 0.4^{\text{a}}$	0.76 ± 0.18	1.3 ± 0.3	1.3 ± 0.2
4	$4.9 \pm 0.3^{\text{a}}$	$6.0 \pm 0.4^{\text{a}}$	0.82 ± 0.1	1.4 ± 0.2	1.4 ± 0.1
5	$7.3 \pm 0.2^{\text{a}}$	$8.9 \pm 0.5^{\text{a}}$	0.82 ± 0.07	1.3 ± 0.1	1.2 ± 0.1
6	7.5 ± 0.5	9.6 ± 0.7	0.78 ± 0.11	2.2 ± 0.3	2.1 ± 0.2
7	9.3 ± 0.9	14.2 ± 1.5	0.65 ± 0.13	2.4 ± 0.4	2.3 ± 0.3
8	11.8 ± 1.5	17.6 ± 2.2	0.67 ± 0.17	2.1 ± 0.6	2.0 ± 0.3

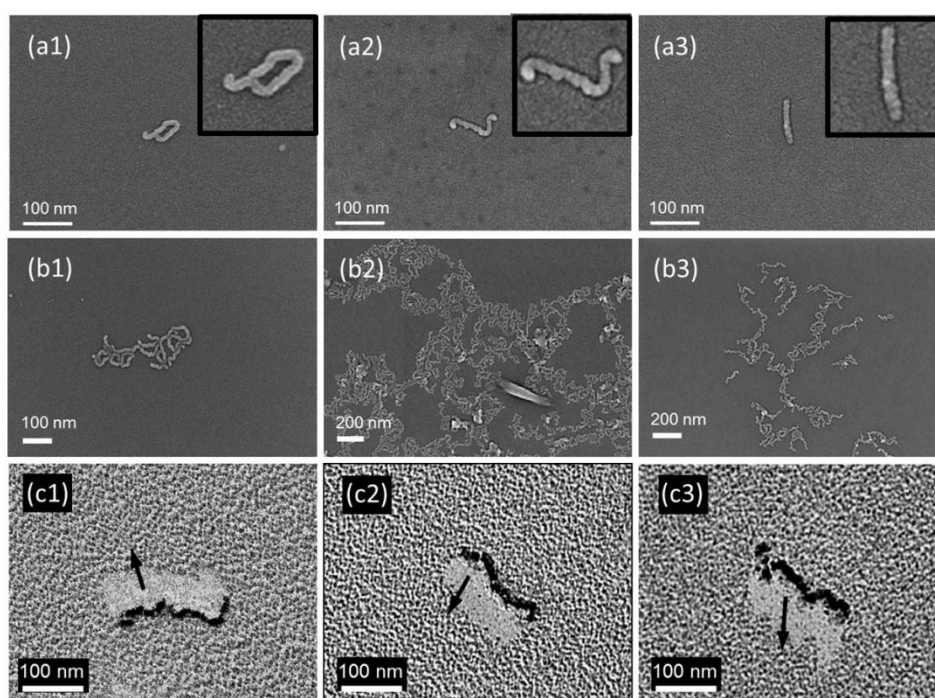


Figure S 9: Sample SEM and TEM images of PG6 (1), PG7 (2), and PG8 (3) from series A. a) SEM images (rotary W shadowed at 45 °C) used for the determination of w_{SEM} ; b) overview SEM images of the samples in subfigures a); c) TEM images used for the determination of h_{TEM} (carbon replicas of samples unidirectionally shadowed at 7 ° elevation angle from the indicated direction).

2.5. ρ_{qSTEM} from STEM-based mass mapping

The following brief description of the qSTEM method of mass determination serves only to provide some basic information; a more in-depth methodological description of modern developments in qSTEM by S. Tacke *et al.* is currently in preparation.

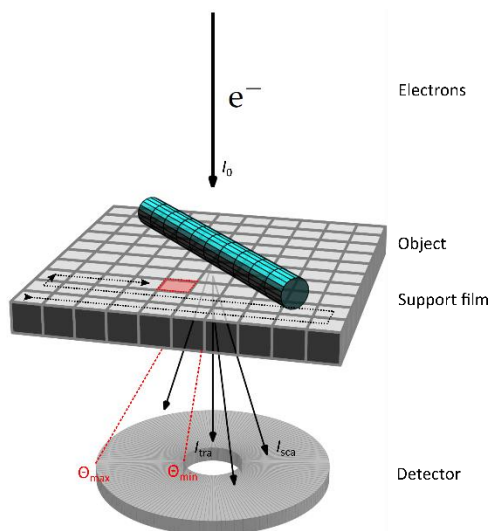


Figure S 10: Schematic representation of qSTEM mass mapping. The sample material, a cylindrical filament deposited on a thin film, is raster scanned by an electron probe. In each point, the electrons are either scattered or transmitted without interaction. If electrons are scattered in a specific angle range (Θ_{\min} to Θ_{\max}), they are detected by an annular dark-field detector. By first approximation, the ratio of measured electron intensity (I_{sca}) vs. impinging intensity (I_0) is proportional to the irradiated mass.

During qSTEM experiments, the sample material is raster scanned with an electron probe (impinging electron current I_0), as illustrated in Figure S 10. In each raster point (pixel), the impinging electrons either interact with the atoms in the underlying volume (voxel) or are transmitted through the sample material without any interaction. In case of an interaction with the sample material, two processes are distinguished: elastic and inelastic scattering. If the sample material is sufficiently thin, multiple-scattering events can be neglected and the relation between I_0 and the scattered intensity I_{sca} can be described by a Lambert-Beer formalism:

$$I_{\text{sca}} = I_0 t \frac{n_t}{V_{\text{voxel}}} \sigma$$

Eq. S 12

Here, I_0 is the incident electron beam intensity, t is the thickness of the sample,^a V_{voxel} is the volume of each voxel, and n_t is the number of atoms in the voxel (with scattering cross-section σ). The mass in the corresponding voxel is defined by $M_{\text{voxel}} = n_t \cdot m_a$, where m_a is the atomic mass. Using the relation $V_{\text{voxel}}/t = A_{\text{pixel}}$ and replacing the atomistic constants m_a and σ by the respective composition-weighted values $\langle m \rangle$ and $\langle \sigma \rangle$, one obtains:

^a For the single-scattering approximation to hold, t must be smaller than the mean free electron path length in a material at the given acceleration voltage (30 kV). For DPs, the mean free path is approximately 30 nm.

$$M_{\text{voxel}} = A_{\text{pixel}} \frac{\langle m \rangle I_{\text{sca}}}{\langle \sigma \rangle I_0}$$

Eq. S 13

For globular proteins, mass determination using Eq. S 13 is fairly straightforward given sufficiently isolated objects on the specimen surface, as the monodisperse particles are identical in mass. Filamentous objects (TMV particles, actin filaments, or indeed DP chains) are rarely of uniform length and mass. It is convenient to determine the mass per unit length M_{qSTEM} instead; Taking the average mass-per-length value from many undisturbed, isolated filament segments (Figure S 11), the density of the filament in question can then be calculated using the cross-section area A_{CS} :

While the above relationships are valid in practice, adjustments to the measured electron current values I_0 and I_{sca} need to be made to account for experimental reality: The incident electron current can fluctuate, which can be corrected for by using the objective aperture current as a reference. Furthermore, not all scattered electrons might be detected by the annular dark-field detector, due to imperfections of the detector, such as the limited active area and quantum efficiency of the detector. Practically, these corrections require detailed knowledge of the operational parameters of the electron microscope, as well as extensive, up-to-date calibration.¹⁵

For the analysis of qSTEM data, the software package MASDET was utilized. A short overview is given here, for details see the corresponding publication by Krzyżánek *et al.*¹⁶ In the first step of data analysis, the images (pixel values) were converted into mass-maps according to Eq. S 13. During this step, the above-mentioned instrumental fluctuations and limitations were taken into account and corrected for. In the next step, regions-of-interest (ROIs) were identified manually and marked by a 90 pixel x 90 pixel box. Figure S 11 shows some examples for each polymer generation. In the following step, the M_{qSTEM} value for each box was calculated. The final value was corrected by taking into account the dose-dependent, beam-induced mass-loss, as determined independently (see Figure S 12).

For the determination of w_{qSTEM} , a software tool was written in LabView, see Figure S 13. The tool is provided for download along with this Electronic Supporting Information. First, ROIs are marked with a box (black box in Figure S 13). For further processing, filaments inside the ROIs are aligned horizontally, line profiles (green lines in Figure S 13) are extracted and averaged. Thereafter, the width of the object is determined by two independent approaches: For the first approach, the averaged profile is fitted by a Gaussian curve and the width (2σ) of the fit is taken as a first result. The second approach uses an edge-detection function implemented in LabView. The function determines the start and the end point of a rising ($x_{\text{start}}^{\uparrow}, x_{\text{end}}^{\uparrow}$) and a falling edge ($x_{\text{start}}^{\downarrow}, x_{\text{end}}^{\downarrow}$) within the averaged profile, see Figure S 14. The distance between the midpoints of both edges determines the width in this case. Finally, the two results are compared and if they agree within a specified error range (in the present case 33%), the results are averaged and saved.

Densities ρ_{qSTEM} were calculated automatically from the M_{qSTEM} values generated in each individual experiment (see Table S 6 & Table S 7) using Eq. S 14, assuming different cross-section geometries (Table S 5). The cross-section areas A_{CS} were calculated using the width values obtained from qSTEM (w_{qSTEM} , Table S 5) and the height values h_{TEM} from other experiments (Table S 4).

$$\rho_{\text{qSTEM}} = \frac{M_{\text{qSTEM}}}{A_{\text{CS}}}$$

Eq. S 14

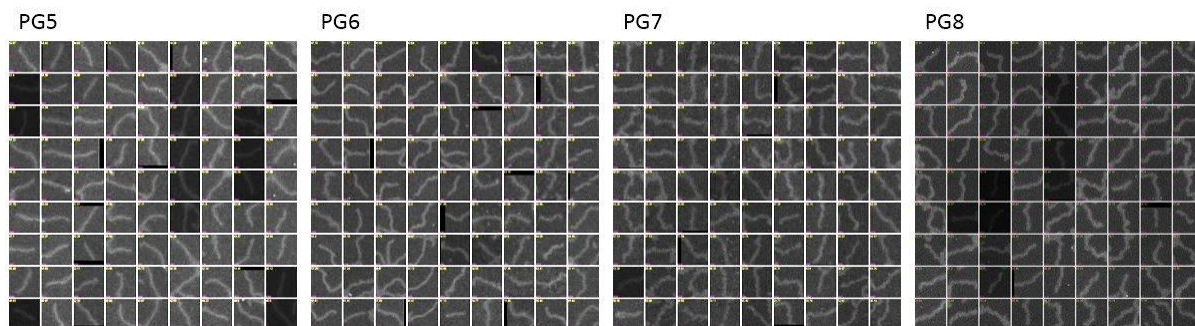


Figure S 11: Gallery of picked particles.

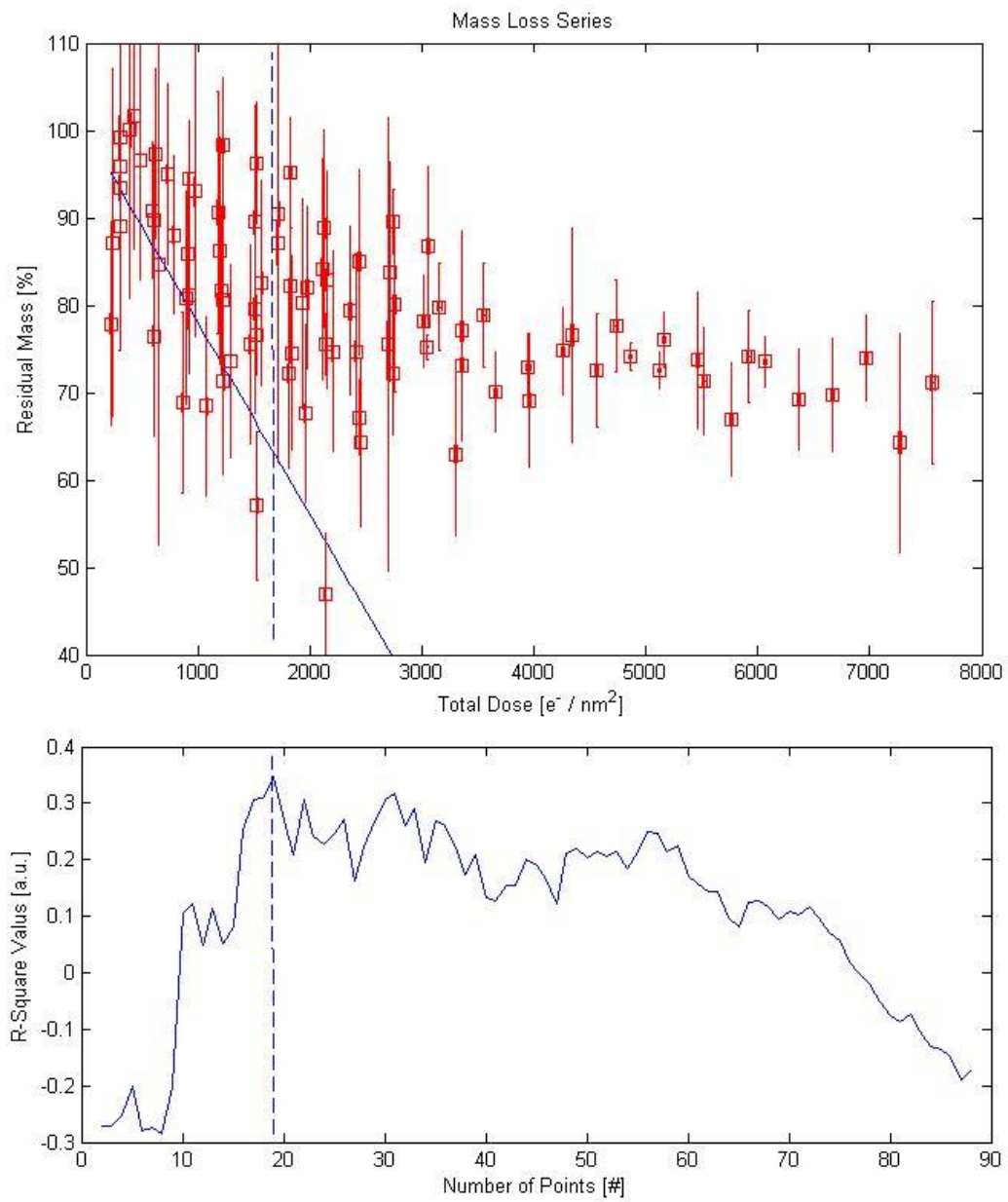


Figure S 12: Combined mass-loss series measurements. The dashed blue line marks the last data point which was included in the linear fit and resulted in the highest R-square value, see also graph at the bottom.

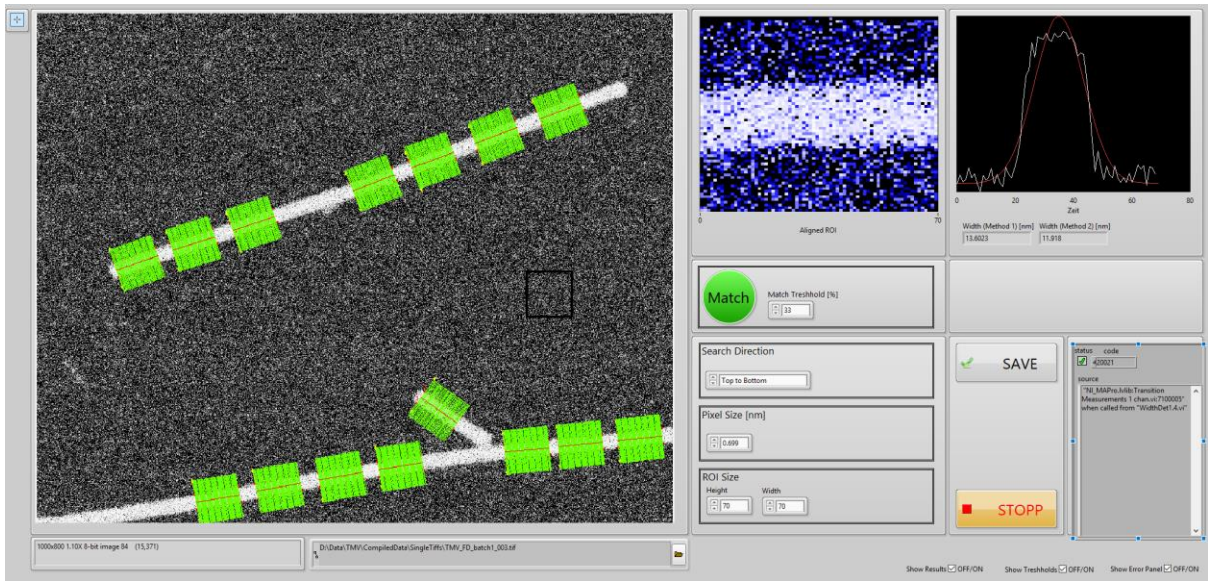


Figure S 13: LabView software for width determination. First, a region-of-interest is marked by the black box. Thereafter, the width of the filament (TMV) is determined by two independent approaches. If both approaches result in the same values (within a tolerance of 33%), both results are averaged and saved.

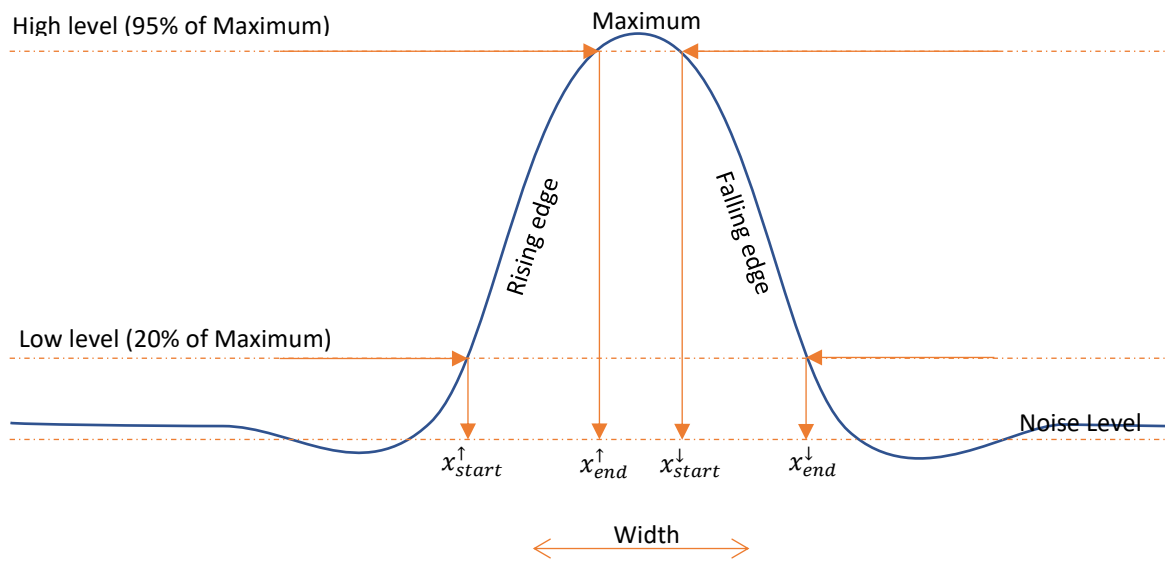


Figure S 14: Edge detection as implemented in LabView.

Table S 5: M_{qSTEM} , w_{qSTEM} and ρ_{qSTEM} values obtained for the DPs from series A. a) The M_{qSTEM} values, widths and corresponding cross-sectional areas were calculated individually for each qSTEM experiment (see Table S 6, Table S 7), the values presented here are the corresponding weighted averages.

<i>g</i>	M_{qSTEM} (kDa nm⁻¹)^a	w_{qSTEM} (nm)^a	ρ_{qSTEM} (g cm⁻³)		
			Rectangle	Sloped (Gaussian)	Cut circle
5	37.8 ± 1.8	8.1 ± 1.8	1.24 ± 0.03	1.29 ± 0.04	1.34 ± 0.04
6	52 ± 3	9.5 ± 2.8	1.21 ± 0.03	1.43 ± 0.05	1.46 ± 0.05
7	52 ± 3	10.6 ± 3.3	0.92 ± 0.03	0.99 ± 0.03	1.32 ± 0.07
8	72 ± 4	10.9 ± 3.9	1.24 ± 0.02	1.08 ± 0.02	1.82 ± 0.11

Table S 6: qSTEM evaluation for a) PG5 and b) PG6 (series A).

a)

PG5											
Data											
ITEM	ΔITEM	WSEM	ΔWSEM	rFW	Δr	SEMI	STD	SEMI	STD	SEMI	STD
7.30	0.20	8.90	0.50	0.82	0.06						
Mass											
ROIS #	MPL	STD	SEMI	Corr.	ΔMPL	Width	STD	SEMI	Corr.	ΔW	Width
#	kDa/nm	kDa/nm	kDa/nm	p(0.005)	p(0.005)	nm	nm	nm	p(0.005)	nm	nm
263	47.59	6.22	0.68	2.64	1.78	2.63	9.87	2.04	0.13	2.60	0.33
762	39.69	7.16	0.44	2.60	1.13	762	8.56	1.30	0.05	2.59	0.12
157	42.94	5.61	1.10	2.79	3.06	157	8.62	1.42	0.16	2.65	0.43
1884	39.33	3.86	0.23	2.60	0.60	1884	7.93	1.29	0.03	2.58	0.09
1161	36.60	3.70	0.14	2.59	0.36	1161	7.48	1.11	0.03	2.58	0.08
1046	37.07	4.40	0.21	2.60	0.54	1046	7.89	1.41	0.04	2.58	0.11
Height											
ROIS #	h()	Δh	h()	Δh	h()	ROIS #	h()	Δh	h()	Δh	h()
#	nm	nm	nm	nm	nm	#	nm	nm	nm	nm	nm
263	7.30	1.07	7.30	1.07	7.30	263	7.30	1.07	7.30	1.07	7.30
762	7.30	0.89	7.30	0.89	7.30	762	7.30	0.89	7.30	0.89	7.30
157	7.30	1.10	7.30	1.10	7.30	157	7.30	1.10	7.30	1.10	7.30
1884	7.30	0.82	7.30	0.82	7.30	1884	7.30	0.82	7.30	0.82	7.30
1161	7.30	0.77	7.30	0.77	7.30	1161	7.30	0.77	7.30	0.77	7.30
1046	7.30	0.82	7.30	0.82	7.30	1046	7.30	0.82	7.30	0.82	7.30
Radius											
ROIS #	R(w)	ΔR	R(w)	ΔR	R(w)	ROIS #	R(w)	ΔR	R(w)	ΔR	R(w)
#	nm	nm	nm	nm	nm	#	nm	nm	nm	nm	nm
263	4.93	0.16	4.93	0.16	4.93	263	4.93	0.16	4.93	0.16	4.93
762	4.28	0.06	4.28	0.06	4.28	762	4.28	0.06	4.28	0.06	4.28
157	5.17	0.13	5.17	0.13	5.17	157	5.17	0.13	5.17	0.13	5.17
1884	3.96	0.04	3.96	0.04	3.96	1884	3.96	0.04	3.96	0.04	3.96
1161	3.74	0.04	3.74	0.04	3.74	1161	3.74	0.04	3.74	0.04	3.74
1046	3.95	0.06	3.95	0.06	3.95	1046	3.95	0.06	3.95	0.06	3.95
Rectangle											
ROIS #	A	ΔA	Density	Δp	Z(f)	A/W(f)	ΔA	Density	Δp	Z(f)	A/W(f)
#	nm ²	nm ²	nm ² g/cm ³	g/cm ³	[a.u.]	nm ²	nm ²	nm ² g/cm ³	g/cm ³	[a.u.]	nm ²
263	97.33	6.44	0.61	0.04	72.02	10.64	1.10	0.10	0.64	60.57	5.46
762	73.35	2.09	0.90	0.02	62.52	7.67	1.05	0.08	0.64	50.57	5.46
157	74.36	7.41	0.95	0.07	62.95	9.13	1.13	0.11	0.64	51.26	5.55
1884	107.08	5.31	0.62	0.03	75.54	11.50	1.17	0.11	0.64	73.82	6.00
1161	62.85	1.42	1.04	0.02	57.87	6.51	1.13	0.09	0.64	43.33	4.69
1046	54.63	5.82	1.11	0.07	54.63	5.82	1.11	0.07	0.64	38.61	4.18
Average	62.30	1.78	0.99	0.02	57.62	6.55	1.07	0.02	0.64	42.95	4.65
Circle											
ROIS #	A	ΔA	Density	Δp	Z(f)	A/W(f)	ΔA	Density	Δp	Z(f)	A/W(f)
#	nm ²	nm ²	nm ² g/cm ³	g/cm ³	[a.u.]	nm ²	nm ²	nm ² g/cm ³	g/cm ³	[a.u.]	nm ²
263	76.40	5.06	1.03	0.05	66.4	67.10	7.27	1.18	0.08	66.4	67.10
762	57.58	1.64	1.14	0.03	66.4	67.10	7.27	1.18	0.08	66.4	67.10
157	59.37	5.82	1.22	0.09	66.4	67.10	7.27	1.18	0.08	66.4	67.10
1884	84.06	4.17	1.05	0.04	66.4	67.10	7.27	1.18	0.08	66.4	67.10
1161	49.33	1.12	1.32	0.02	66.4	67.10	7.27	1.18	0.08	66.4	67.10
1046	45.96	0.99	1.38	0.02	66.4	67.10	7.27	1.18	0.08	66.4	67.10
Average	48.91	1.40	1.26	0.02	66.4	67.10	7.27	1.18	0.08	66.4	67.10
Triangle											
ROIS #	A	ΔA	Density	Δp	Z(f)	A/W(f)	ΔA	Density	Δp	Z(f)	A/W(f)
#	nm ²	nm ²	nm ² g/cm ³	g/cm ³	[a.u.]	nm ²	nm ²	nm ² g/cm ³	g/cm ³	[a.u.]	nm ²
263	36.01	5.42	2.19	0.21	36.01	5.42	2.19	0.21	36.01	5.42	2.19
762	31.26	3.93	2.11	0.16	31.26	3.93	2.11	0.16	31.26	3.93	2.11
157	31.47	4.56	2.27	0.22	31.47	4.56	2.27	0.22	31.47	4.56	2.27
1884	37.77	5.75	2.34	0.22	37.77	5.75	2.34	0.22	37.77	5.75	2.34
1161	28.94	3.26	2.26	0.15	28.94	3.26	2.26	0.15	28.94	3.26	2.26
1046	27.31	2.91	2.23	0.14	27.31	2.91	2.23	0.14	27.31	2.91	2.23
Average	29.81	3.27	2.14	0.15	29.81	3.27	2.14	0.15	29.81	3.27	2.14
Gaussian Profile (68.2%)											
ROIS #	A	ΔA	Density	Δp	Z(f)	A/W(f)	ΔA	Density	Δp	Z(f)	A/W(f)
#	nm ²	nm ²	nm ² g/cm ³	g/cm ³	[a.u.]	nm ²	nm ²	nm ² g/cm ³	g/cm ³	[a.u.]	nm ²
263	61.56	15.94	1.28	0.20	61.56	15.94	1.28	0.20	61.56	15.94	1.28
762	53.44	6.19	1.23	0.09	53.44	6.19	1.23	0.09	53.44	6.19	1.23
157	53.81	22.17	1.33	0.33	53.81	22.17	1.33	0.33	53.81	22.17	1.33
1884	64.57	14.07	1.37	0.18	64.57	14.07	1.37	0.18	64.57	14.07	1.37
1161	49.47	4.59	1.32	0.07	49.47	4.59	1.32	0.07	49.47	4.59	1.32
1046	46.69	4.09	1.30	0.07	46.69	4.09	1.30	0.07	46.69	4.09	1.30
Average	49.25	5.32	1.25	0.08	49.25	5.32	1.25	0.08	49.25	5.32	1.25

b)

PG6											
Data											
ITEM	ΔITEM	WSEM	ΔWSEM	rFW	Δr	SEMI	STD	SEMI	STD	SEMI	STD
7.50	0.50	9.60	0.70	0.78	0.10						
Mass											
ROIS #	MPL	STD	SEMI	Corr.	ΔMPL	Width	STD	SEMI	Corr.	ΔW	Width
#	kDa/nm	kDa/nm	kDa/nm	p(0.005)	p(0.005)	nm	nm	nm	p(0.005)	nm	nm
224	54.16	10.45	1.22	2.65	3.22	224	9.60	1.73	0.12	2.60	0.30
403	51.51	7.80	0.81	2.63	2.14	403	9.10	1.72	0.09	2.59	0.22
500	47.48	6.12	0.55	2.63	1.45	500	8.08	1.16	0.05	2.59	0.13
1284	47.08	5.71	0.35	2.60	0.91	1284	8.29	1.69	0.05	2.58	0.12
945	53.84	8.06	0.46	2.60	1.19	945	10.34	1.64	0.05	2.59	0.14
346	113.90	8.78	0.83	2.61	2.15	346	10.45	1.77	0.10	2.59	0.25
541	54.13	7.28	0.60	2.61	1.57	541	10.12	2.02	0.09	2.59	0.22
559	57.96	6.74	0.61	2.61	1.60	559	10.49	1.88	0.08	2.59	0.21
Average	1242	51.48	0.62	2.77		Average	9.56				
Height											
ROIS #	h()	Δh	h()	Δh	h()	ROIS #	h()	Δh	h()	Δh	h()
#	nm	nm	nm	nm	nm	#	nm	nm	nm	nm	nm
224	7.50	1.04	7.50	1.04	7.50	224	7.50	1.04	7.50	1.04	7.50
403	7.50	0.97	7.50	0.97	7.50	403	7.50	0.97	7.50	0.97	7.50
500	7.50	0.85	7.50	0.85	7.50	500	7.50	0.85	7.50	0.85	7.50
1284	7.50	0.86	7.50	0.86	7.50	1284	7.50	0.86	7.50	0.86	7.50
945	7.50	1.06	7.50	1.06	7.50	945	7.50	1.06	7.50	1.06	7.50
346	7.50	1.10	7.50	1.10	7.50	346	7.50	1.10	7.50	1.10	7.50
541	7.50	1.07	7.50	1.07	7.50	541	7.50	1.07	7.50	1.07	7.50
Average	7.50	1.09	7.50	1.09	7.50	Average	7.50	1.09	7.50	1.09	7.50
Radius											
ROIS #	R(w)	ΔR	R(w)	ΔR	R(w)	ROIS #	R(w)	ΔR	R(w)	ΔR	R(w)
#	nm	nm	nm	nm	nm	#	nm	nm	nm	nm	nm
224	4.80	0.15	4.80	0.15	4.80	224	4.80	0.15	4.80	0.15	4.80
403	4.55	0.11	4.55	0.11	4.55	403	4.55	0.11	4.55	0.11	4.55
500	4.04	0.07	4.04	0.07	4.04	500	4.04	0.07	4.04	0.07	4.04
1284	4.14	0.06	4.14	0.06	4.14	1284	4.14	0.06	4.14	0.06	4.14
945	5.17	0.07	5.17	0.07	5.17	945	5.17	0.07	5.17	0.07	5.17
346	5.22	0.12	5.22	0.12	5.22	346	5.22	0.12	5.22	0.12	5.22
541	5.06	0.11	5.06	0.11	5.06	541	5.06	0.11	5.06	0.11	5.06
Average	5.24	0.10	5.24	0.10	5.24	Average	5.24	0.10	5.24	0.10	5.24
Rectangle											
ROIS #	A	ΔA	Density	Δp	Z(f)	A/W(f)	ΔA	Density	Δp	Z(f)	A/W(f)
#	nm ²	nm ²	nm ² g/cm ³	g/cm ³	[a.u.]	nm ²	nm ²	nm ² g/cm ³	g/cm ³	[a.u.]	

3. Density Values Obtained for Series B

For series B, samples of PG5 (differing slightly in chemical structure⁴ from the analogous members series A, see Scheme S 1), PG6, PG7, and PG8 were investigated. The $g > 5$ series B DPs are of higher structural perfection than the corresponding members of series A (see Table S 1, Table S 2). The investigations of series B were limited to high g DPs since the members of $g = 1 - 4$ were prepared in the same manner for both series and did not differ significantly in terms of defect frequency (compare Table S 1 with Table S 2). As ρ_{bulk} sets a lower limit for individual-molecule density values and as ρ_{SAXS} resulted in the most extreme density values for the DPs from series A, the investigations of series B were limited to density gradient column (Table S 8) and SAXS measurements (Table S 8, Figure S 15, Figure S 16). The improved structural perfection of the high g members of series B was hoped to eliminate some of the uncertainties associated with M_{label} in particular (see section 4.1).

As the comparison of values for series A and B in Figure S 17a shows, the values of ρ_{bulk} in series B are slightly above those for DPs from series A, with the exception of PG8. Interestingly, this trend is paralleled by values of ρ_{SAXS} , as evident in Figure S 17b, though the drop-off for PG8 in that case is much larger. The latter observation is likely at least in part the result of the rather broad scattering peaks, which render accurate peak assignment more difficult. The poorly resolved scattering for PG7 and particularly PG8 from series B (Figure S 15, Figure S 16) when compared to the corresponding samples in series A (see Figure S 6) might be a consequence of the shape transition discussed elsewhere,⁴ which is thought to result from the transition to $g > g_{\text{max}}$ molecular objects. Such corrugation would make it more difficult for the individual molecules to pack regularly and would result in on average larger spacing between individual chains, as observed for PG8 in series B (Table S 8).

Table S 8: ρ_{bulk} (average of three measured pills each), SAXS unit cell parameters and ρ_{SAXS} obtained for DPs from series B.

g	ρ_{bulk} (g cm ⁻³)	oblique				tetragonal		hexagonal		rhombohedral		
		a (nm)	b (nm)	γ (°)	ρ_{SAXS} (g cm ⁻³)	a (nm)	ρ_{SAXS} (g cm ⁻³)	a (nm)	ρ_{SAXS} (g cm ⁻³)	a (nm)	γ (°)	ρ_{SAXS} (g cm ⁻³)
5	1.25	9.50	5.21	48	1.86	7.09	1.37	8.18	1.19	9.43	49	1.03
6	1.24	9.96	5.56	51	3.38	7.70	2.44	8.89	2.11	9.69	53	1.94
7	1.23	9.30	5.26	59	6.78	8.00	4.46	9.24	3.86	9.70	56	3.68
8	1.20	25.17	19.94	27	1.59	11.48	2.76	13.26	2.39	11.73	78	2.71

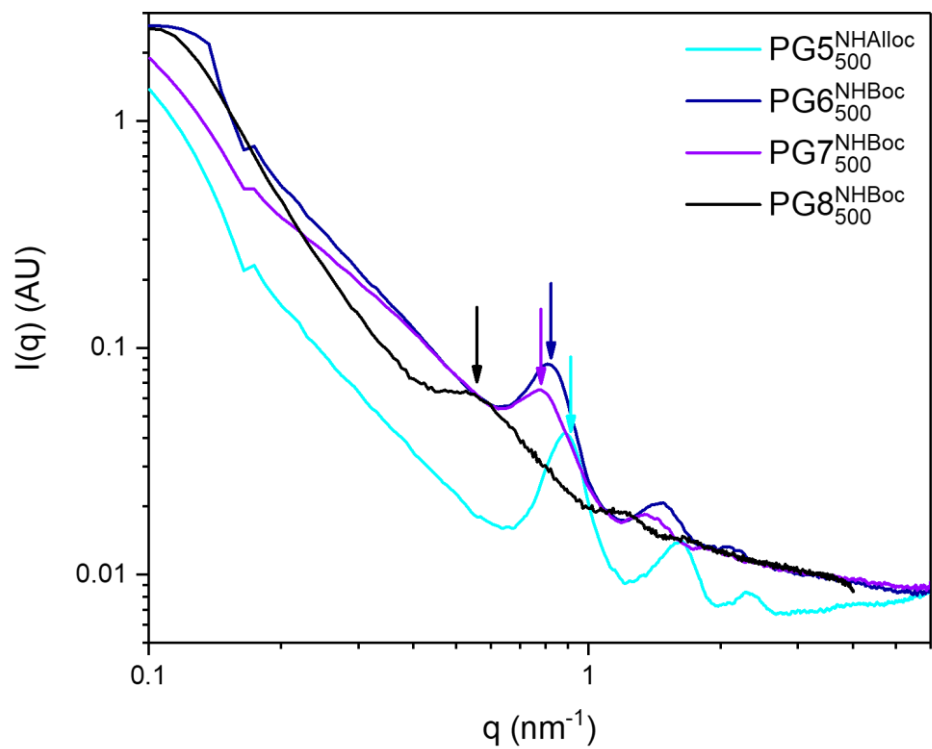


Figure S 15: Overlay of the SAXS curves obtained for DPs from series A.

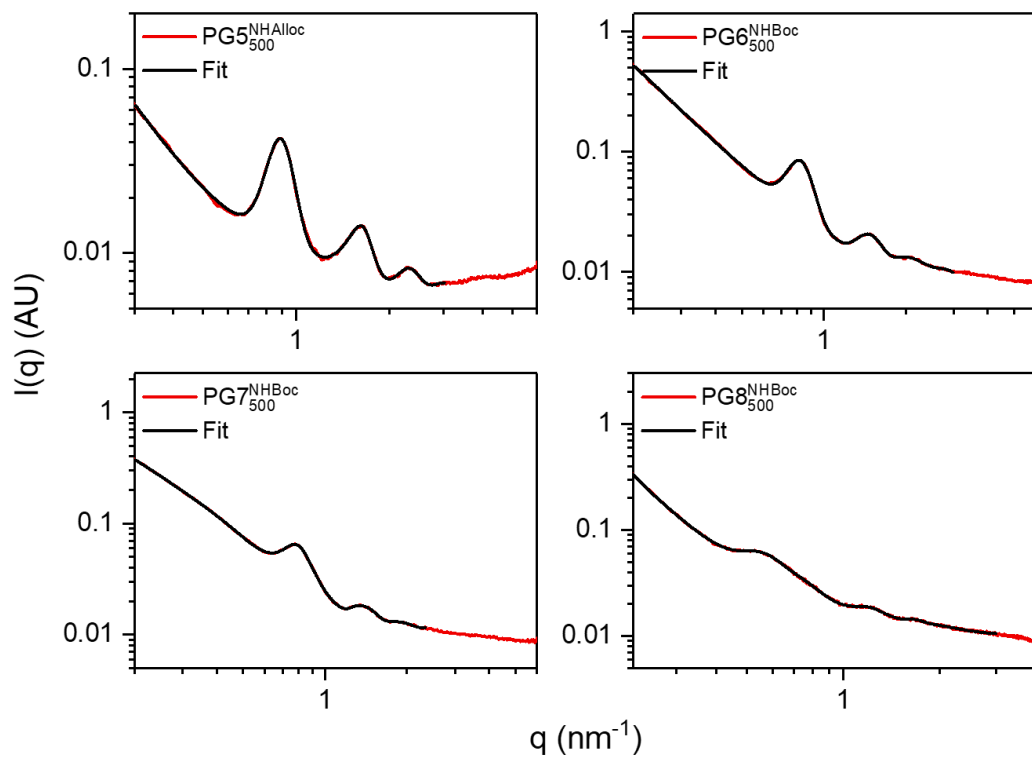


Figure S 16: SAXS curves and curve fits (columnar rhombohedral packing) for DPs from series B.

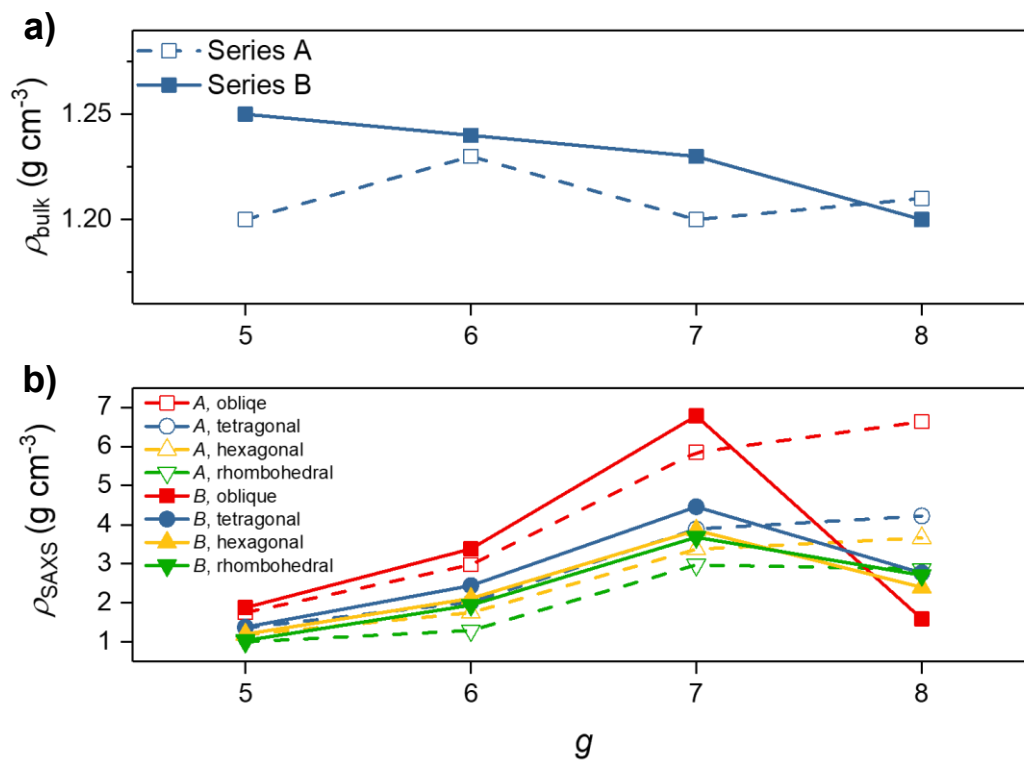


Figure S 17: Density values a) ρ_{bulk} (density gradient column measurements) and b) ρ_{SAXS} for DPs from series B (solid lines) in comparison to the values obtained for the corresponding members of series A (dashed lines; see main text, Fig. 3, Tab. 1; this SI, Figure S 5, Table S 3)

4. Discussion of Potential Sources of Error in the Determination of Density Values

This section contains a discussion of the factors potentially affecting the determination of ρ values, as listed in Tab. 2 (see main text), which is reprinted below for ease of reference (Table S 9). This concerns first the necessary inputs for the calculation of ρ_{SAXS} , $\rho_{\text{SEM/TEM}}$ and ρ_{qSTEM} which are of overarching concern, and then potential sources of error and uncertainty as they apply to the individual methods. This discussion is limited to the DPs from series A; most aspects discussed below apply to the DPs of series B, as well, with the significant exception of $\langle M_g \rangle$, values of which are likely closer to the ideal (M_g^{max}) than for the DPs from series A, eliminating some factors of uncertainty.⁴

Table S 9: Key features and deficiencies of the approaches to density determination employed in this publication (see main text, Tab. 2).

Method	Information gained from measurement	Inputs for density calculation	Other potential sources of error/points of note
Hydrostatic weighing	envelope density	-	- Proportion of ordered domains - Voids
Density gradient column	envelope density	-	- Proportion of ordered domains - Voids
SAXS	self-assembled domain unit cell	MPL; packing model	-
SEM/TEM	SEM: width (w_{SEM}) TEM: height (h_{TEM})	MPL; chain cross-section	- Thresholding (h_{TEM} & w_{SEM}) - Measurements on “bumpy” objects (h_{TEM} & w_{SEM}) - Metal coating layer thickness (w_{SEM}) - Cross-section model - Two different series of measurements & DPs - Flattening on mica vs. carbon
qSTEM	molar mass per unit length (MPL); width	height; chain cross-section	- Thresholding - Height input (h_{TEM})

4.1. MPL values for the derivation of ρ_{SAXS} and $\rho_{\text{SEM/TEM}}$

At given unit cell/individual molecule dimensions, a ready explanation for the extraordinarily high density values obtained for $g > 6$ DPs would be a lower than assumed mass per length value M_{label} . This would correspond to larger mass deficiencies than those noted in Table S 1. While $\langle M_g \rangle$ as obtained from the labelling of structural defects is likely reliable for $g < 7$, the values for PG7 and PG8 are likely overestimates, as the defect labelling method begins to fail for structures of high steric congestion – as is the case for these $g > g_{\text{max}}$ DPs.⁴

In Table S 10, molar masses per repeat unit from Table S 1 and those obtained from qSTEM mass mapping are compared with those *calculated* to obtain a “reasonable” density value of $\rho = 1.5 \text{ g cm}^{-3}$ at given chain dimensions from SAXS or SEM/TEM measurements for the DPs of $g > 4$. Table S 10 also gives the corresponding values of the parameter α (Eq. S 15, where M is a generic molar mass value) which serves as a measure of structural perfection (see Ref. 4 for a more in-depth discussion). Particularly for qSTEM and SAXS measurements, very low values down to $\alpha < 0.5$ are reached. Another point of note is the course of $M_{\text{SAXS}}^{\text{calc}}$, which *decreases* slightly from PG6 to PG7; similarly, M_{qSTEM} and the corresponding mass per repeating unit $M_{\text{qSTEM}}^{\text{calc}}$ suggests that PG7 has nearly the same molar mass as PG6.

$$\alpha = \frac{M}{M_g^{\text{max}}}$$

Eq. S 15

Values of α as low as α_{SAXS} and α_{qSTEM} in Table S 10 would correspond to very large numbers of defects. Prior evidence suggested that the defect labelling method used in the derivation of $\langle M_g \rangle$ does start to fail at $g \approx 7$,^{2,4} but the requirement for this failure is extreme steric congestion, such that defects (remaining free amines) are not accessible for labeling, anymore. DPs bearing as many defects as α_{SAXS} and α_{qSTEM} suggest would have very loose structures. DPs with that many free amines would likely be difficult to isolate by chromatographic workup in methylene chloride, during which substances with many amino groups would adhere to the silica gel, if they are soluble at all. The seeming dip in molar mass obtained by back-calculation of $M_{\text{SAXS}}^{\text{calc}}$ is also not supported by experiment: Other data (including synthetic yields $> 50\%$,⁴ molar mass increases in GPC,^{2,4} and increasing physical dimensions in AFM,² SEM and TEM) support the expected significant *increase* in molar mass.

Independent data for the molar mass and molar mass distribution of DP repeating units is unfortunately only available for products of the partial degradation of PG5, PG6, and PG7: Mass spectrometric evidence for PG5 suggests near-monodisperse repeating units with very few defects, and GPC data for PG5-PG7 shows clear increases in the molar mass of the repeating unit.^{5,6} Overall, deviations in M_{exp} on the order of -20% are within the realm of possibility for PG7 and PG8, but values of $\alpha < 0.7$ appear unrealistic, nevertheless.

Table S 10: Ideal, experimental and calculated molar masses per repeat unit and corresponding α values for PG5 – PG8 (series A). a) Cut circular cross-section, $\rho = 1.5 \text{ g cm}^{-3}$; b) columnar rhombohedral phase, $\rho = 1.5 \text{ g cm}^{-3}$; c) cut circle cross-section, $\rho = 1.5 \text{ g cm}^{-3}$. Values of $\alpha > 1$ may result from d) effective DP densities of $\rho < 1.5 \text{ g cm}^{-3}$ or e) from the failure of Sanger labelling.^{2,4}

g	M_{exp} [g mol ⁻³]	$\langle M_g \rangle$ [g mol ⁻³]	α_{Sanger}	$M_{\text{qSTEM}}^{\text{calc a)}$ [g mol ⁻³]	α_{qSTEM}	$M_{\text{SAXS}}^{\text{calc b)}$ [g mol ⁻³]	α_{SAXS}	$M_{\text{SEM/TEM}}^{\text{calc c)}$ [g mol ⁻³]	$\alpha_{\text{SEM/TEM}}$
5	10952	10952	0.99	9526	0.86	13345	1.21 ^{d)}	12435	1.13 ^{d)}
6	21969	20016	0.90	12978	0.58	23253	1.05 ^{d)}	13815	0.62
7	40492	40492	0.93	13180	0.30	20453	0.47	25029	0.58
8	55325	78896	1.43 ^{e)}	18320	0.33	28844	0.52	39485	0.71

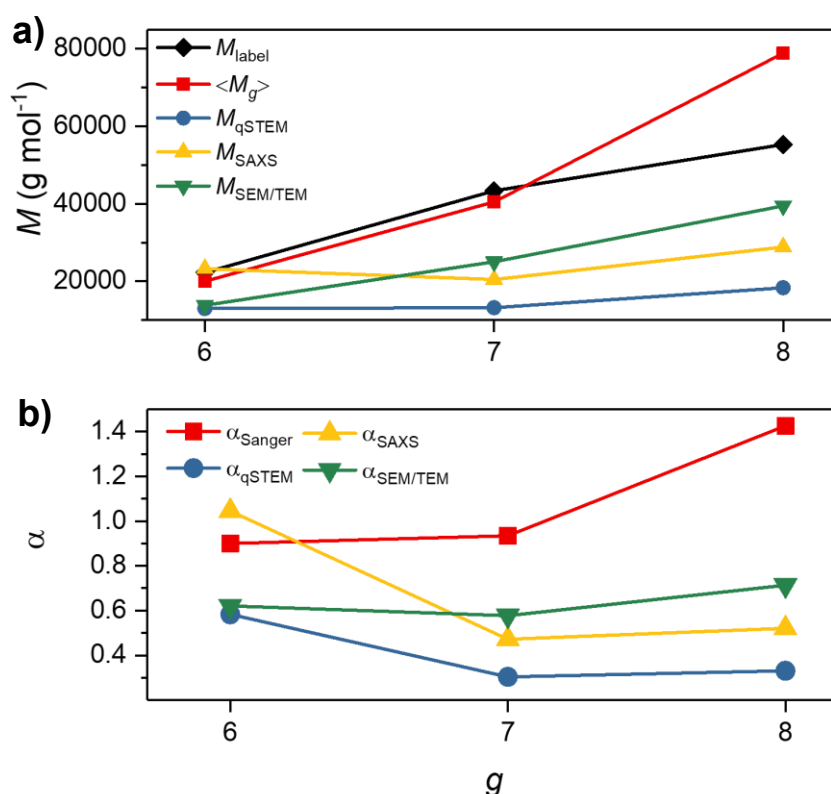


Figure S 18: a) Molar mass values and b) values of α from Tab. S11.

The MPL values implicit in Eq. S 11 and Eq. S 7 are not only dependent on the effective M , but also on the length of the repeat unit L_{RU} . With a value of $L_{\text{RU}} = 0.252 \text{ nm}$, an essentially stretched out, all trans zig-zag DP backbone was assumed. While this is likely realistic particularly for DPs of $g > 4$, effective values may be lower for low g DPs, as reflected by their lower persistence lengths.¹ In view of the uncertainties associated with molar masses per repeat unit, no g -dependent correction was applied in this case, however. In sterically strongly congested structures such as DPs, one could image backbone bonds being stretched beyond the normal average for polymer backbone C-C bonds. Indications of this can be found in previous molecular dynamics simulations,^{17,18} which indicated a) that perfect DPs of $g > 6$ feature unreasonably stretched C-C backbone bonds and that b) already at $g = 5$ there is some stretching of the individual bonds. As it was recently found that an extension of the backbone by $\sim 10\%$ due to swelling of the dendritic periphery is related to mechanochemical activation and scission of the DP backbone,⁶ more substantial backbone stretching appears improbable. In combination with the potential error margins for M_{exp} discussed above, overall the deviation of the

MPL value M_{label} might amount to $\sim -25\%$ for PG7 and PG8. While this is substantial, it is still insufficient to explain the extraordinarily large density values obtained in particular from SAXS measurements.

4.2. Chain cross-section models for the derivation of ρ_{SAXS} , $\rho_{\text{SEM/TEM}}$ and ρ_{qSTEM}

Models of possible chain cross-sections or space-filling models are a factor of significant uncertainty in the determination of ρ based on microscopic parameters, as there is currently no independent verification for the assumed cross-sections.

For deposited specimen, methods to gain access to cross-section geometry have been suggested in the Outlook section of the main text: Electron tomography or the imaging of coated, cross-sectionally cut specimen by SEM may give access to the desired information. For the present publication however, cross-section models had to be assumed. Within experimentally determined dimensions h and w (*i.e.* h_{TEM} , w_{SEM} , w_{qSTEM} , h_{AFM} , w_{AFM} ,¹⁰ *etc.*) the extremes of possible cross-section geometries for deposited filaments are the ellipse (Figure S 19a, having the lowest possible cross-section area for a compact cross-section) and the rectangle (Figure S 19d, having the largest possible cross-section area). These extremes are physically improbable: Figure S 19a represents an object which is in contact with its substrate through a mere geometric line; a substantial contact area is much more probable. Figure S 19d is equally improbable: A strongly angular shape presents an unfavourably large surface area exposed to vacuum. More compact shapes within the given confines of height and width are more likely, as shown in Figure S 19b for a cut circular and in Figure S 19c for a sloped cross-section. Among these two models, the cut circular model Figure S 19b) was preferred for the evaluation of qSTEM and SEM/TEM results, as an analytical expression for the cross-section area exists (Eq. S 9), and as it is a likely shape for deposited DPs in particular: The dendritic side chains are very compact and quite tightly packed. The formation of adsorbates of this geometry on mica has also been suggested by MD simulations.¹⁴ Sloped shapes (Figure S 19c) are more difficult to evaluate: While possible in principle *e.g.* from qSTEM mass maps (see section 2.4), many different profile shapes might be assumed.^b

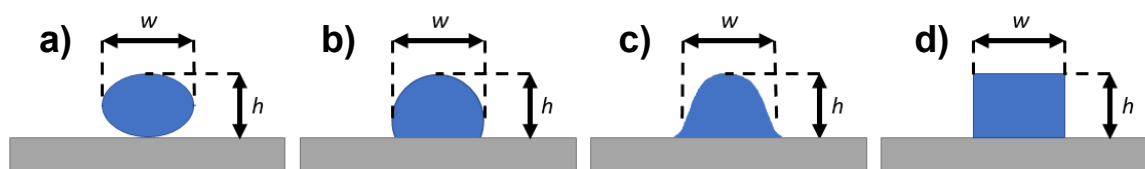


Figure S 19: Range of prototypical cross-section models shown for identical values of w and h : a) ellipse; b) cut circle; c) slope; d) rectangle.

It should be noted that the cross-section of a deposited chain likely depends to some degree on the substrate. This was previously investigated in some depth for DPs of up to $g = 5$.¹⁰ The cited study found only minor differences in widths, comparing submonolayers of DPs adsorbed on mica, HOPG and amorphous carbon by SEM and AFM. h_{AFM} values were found to differ slightly, HOPG providing larger heights than mica. This suggests a slight shift within the continuum of model cross-sections in Figure S 19: On mica, a more sloped shape may be preferred, providing a larger area of contact with the strongly interacting substrate, whereas weakly interacting HOPG may lead to a more closely cut-circular cross-section. This behavior parallels substrate interactions found for stiff biological specimen such as TMV,¹⁹ but differs significantly from that of bottle-brush polymers, which flatten out substantially upon strong adhesion, due to their more flexible and less compact side chain structures.¹³

^bThe issue of thresholding is discussed in the context of the discussion of qSTEM measurements, see section 4.6.

For bulk DPs, the chain cross-section depends on DP-DP interactions. A factor in the interpretation of SAXS results is therefore the volume occupancy of the given unit cell, *i.e.* the degree of interdigitation between neighboring DP chains. The two extremes are represented in Figure S 20: Hard, cylinders (Figure S 20a) and completely contacted DPs, effectively filling the unit cell homogeneously (Figure S 20c). DPs possess some degree of flexibility (see SEM/TEM results, Table S 4) and rheological investigations have demonstrated substantial interdigitation.^{11,20} In addition to this, the low-interaction extreme (Figure S 20a) is made improbable by large surface area exposed to vacuum and large internal voids. A more realistic case is represented schematically in Figure S 20b: Some density fluctuations are present within the unit cell, but the chains are significantly deformed away from the ideal cylindrical shape, and there is substantial contact area *e.g.* for interdigitation. The volume occupancy in the ordered domains of the annealed samples is likely quite high (> 95 %).

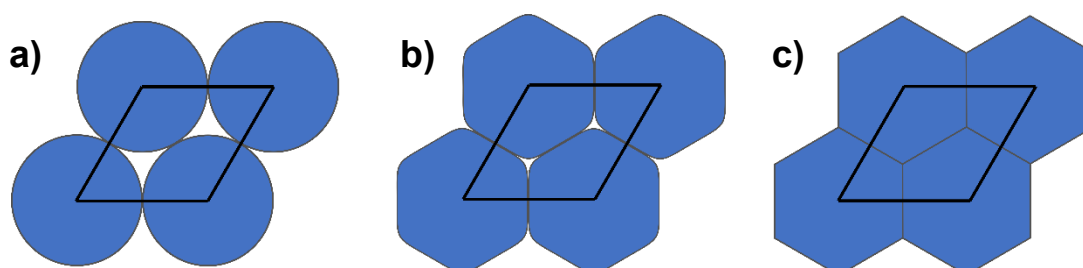


Figure S 20: Range of volume occupancies for identical unit cell dimensions (shown for columnar hexagonal geometry); a) hard cylinders; b) partial interdigitation; c) complete, uniform space filling. Blank spaces are not necessarily empty, but may represent regions of locally lower density.

Differences in space filling can therefore account only for variations in ρ on the order of $\pm 10\%$ - a factor of much greater impact is the unit cell geometry (see section 2.2, Figure S 5). The unit cell is probably of oblique, rhombohedral or hexagonal geometry, the tetragonal case being less likely. Rhombohedral geometry provides the best curve fits (see Figure S 6), and interestingly result in the lowest density values. The precise geometry in the bulk state could unfortunately not be verified externally: Thin sections of PG5^{NHAlloc} were readily prepared.^c However, negative staining with OsO₄ (applied either as an aqueous solution or as a vapor) provided only very weak and no differential contrast, without revealing any structural features. This does however confirm the above notion that the samples are strongly interdigitated and quite densely packed.

^c This polymer (PG5 from series B) was selected for its large number of (unsaturated) NHAlloc groups, which were hoped to be amenable to staining.

4.3. Sources of error & uncertainty for ρ_{bulk}

As no model assumptions are necessary to determine bulk density values, either by hydrostatic weighing or by density gradient column measurements, the variability in ρ_{bulk} is largely due to variability in the measurements themselves. The precision of density gradient column measurements is largely dependent on the reproducibility of positional read-outs, which was determined to be in the range of ± 0.3 mm, translating to standard deviations for individual DP pills of $\delta(\rho_{\text{bulk}}) < 0.005$ g cm⁻³; differences between individual pill densities are much larger. For hydrostatic weighing, the errors are larger ($\delta(\rho_{\text{bulk}}) \approx 0.01 - 0.04$, depending on the precise sample) as the sample mass of the DP pills ($\sim 10 - 30$ mg) was at the lower end of feasibility for this method and the stability of the analytical balance employed in these measurements.

As indicated in the main text, the translation of these bulk density values to individual molecule densities is subject to far larger possible variation, as the overall volume occupancy in the bulk DP pills is unknown. Neither the overall proportion of self-assembled domains probed in SAXS nor the average volume occupancies in self-assembled or amorphous domains are presently known, though the overall “softness” of the DP chains, the careful annealing procedure minimizing internal voids, and the DPs’ tendency for interdigitation all suggest high values of overall volume occupancies (*e.g.* > 95 %).

4.4. Sources of error & uncertainty for ρ_{SAXS}

In addition to the already discussed overarching factors of chain packing model and M_{label} input (sections 4.1 & 4.2), little additional uncertainty arises, as the SAXS evaluation method outlined in section 2.3 relies on a simple peak fit procedure followed by solving a simple system of equations that take the form of Eq. S 5.

4.5. Sources of error & uncertainty for $\rho_{\text{SEM/TEM}}$

A source of uncertainty, represented by the growing error bars for DPs of $g > 5$, is the (in)homogeneity of the DP chain contour, affecting the precision achieved in the determination of both h_{TEM} and w_{SEM} . This corrugation was observed in previous studies and has two potential sources: For series A, defects introduced in the synthesis of PG6 are likely propagated in the preparation of PG7 and PG8, leading to chunks of dendritic matter missing and consequently to an inhomogeneous chain diameter.² A second factor is increasing steric congestion. Data from cryo-TEM in solution²¹ and from AFM of deposited specimen⁴ for DPs from series B suggest that the observed corrugation is due to locally high curvature even in structurally fairly perfect DPs, rather than due to inhomogeneous chain diameters. Considering the increasing aspect ratios observed for deposited DPs of $g > 5$ however (see Table S 4), the second factor is likely of lesser importance for series A.

Another source of potential error is the thickness of the tungsten coating applied by rotary shadowing. The currently used correction of $- 0.7$ nm to w_{SEM} is empirical^{10,12} and subject to experimental variation.

Lastly, note should be made not regarding methodological issues, but the logistics of the specific measurements reported here: The DPs of $g = 1 - 5$ had been investigated in an earlier set of experiments discussed extensively elsewhere;¹⁰ the DPs of $g = 6 - 8$ were studied independently at a

later point. Though the methods employed were identical and though all steps were conducted carefully by qualified personnel, with the specific goal of comparing the “old” and “new” sets of values, shifts in instrumental parameters and other systematic errors can presently not be fully excluded.

4.6. Sources of error & uncertainty for ρ_{qSTEM}

While qSTEM data provides the width value w_{qSTEM} (see Table S 5 and discussion in section 4.6), it does not afford a corresponding height value. To provide the necessary input for the calculation of the chain cross-section area, the values obtained from TEM imaging of W-shadowed DPs (h_{TEM}) were used (Table S 4). A potential issue with this approach are differences in substrates: h_{TEM} values were obtained from DPs deposited on mica, whereas the substrate for qSTEM consisted of a thin film of amorphous carbon. As discussed in section 4.2, the substrate may impact the cross-section geometry and has previously been shown to affect the height of adsorbed DPs.¹⁰ As amorphous carbon is a less strongly interacting substrate than mica, it seems likely that for the present specimen h_{TEM} is a slight underestimate compared to the actual dimensions of the deposited DP specimen investigated by qSTEM mass mapping.

Another factor is the poor contrast in the low-dose qSTEM mass maps. Thresholding during the evaluation of density profiles likely leads to w_{qSTEM} values which are lower than the actual physical dimensions of the DP. The shadowing technique used to determine h_{TEM} on the other hand produces sharp edges which can be imaged at higher electron doses, and therefore thresholding is not as critical. A value with an intensity threshold similar to w_{qSTEM} would likely be smaller than the DPs' actual physical dimensions, *i.e.* it might be close to h_{TEM} as obtained from a more strongly interacting substrate. These two counter-running effects make it difficult to judge whether the use of h_{TEM} introduces an error in either direction, and therefore no corresponding correction was employed in the present data evaluation.

Thresholding of course also affects the determination of M_{qSTEM} : The low-dose protocol necessary to avoid radiation damage (and accompanying mass loss) during mass mapping results in low contrast because the thin amorphous carbon substrate scatters electrons, as well. The low contrast provides no clear, sharp boundaries for the DPs, and therefore the qSTEM evaluation protocol (see section 2.4) incorporates a thresholding algorithm, which determines a cutoff for MPL calculations. This likely results in the loss of some information at the edges of the DP chains, partially explaining the deviations of M_{qSTEM} from M_{label} . The relative deviation does not remain constant, but increases substantially with g (Table S 10), which in part may be due to the increasing flattening of the DPs, as observed for $g > 5$ by SEM/TEM (see Table S 4). A more spread-out adsorbate is subject to greater proportions of its mass being cut off by the thresholding algorithm. This issue should be significantly reduced in the more structurally perfect analogous DPs from series B, which are expected to flatten out less than PG6-PG8 from series A.

5. Additional SAXS and WAXS results

Figure S 21 shows preliminary SAXS results obtained for freeze-dried DP powders; for the intermediate g range (PG4 – PG6), some structured scattering is already evident, but in all cases the improvement achieved by compaction and annealing is substantial (compare with Fig. 2b in the main text and Figure S 6).

In conjunction with SAXS measurements, the wide-angle range was also covered for the DPs from series A. The WAXS signals in Figure S 22 do not reveal any clear signs of side-chain crystallinity, and the DPs are accordingly intramolecularly largely amorphous. Furthermore, the average intramolecular correlations obtained from WAXS curve fits as noted in Figure S 22 do not change significantly with g – the small numerical shifts noted in Figure S 22 are well within experimental tolerance.

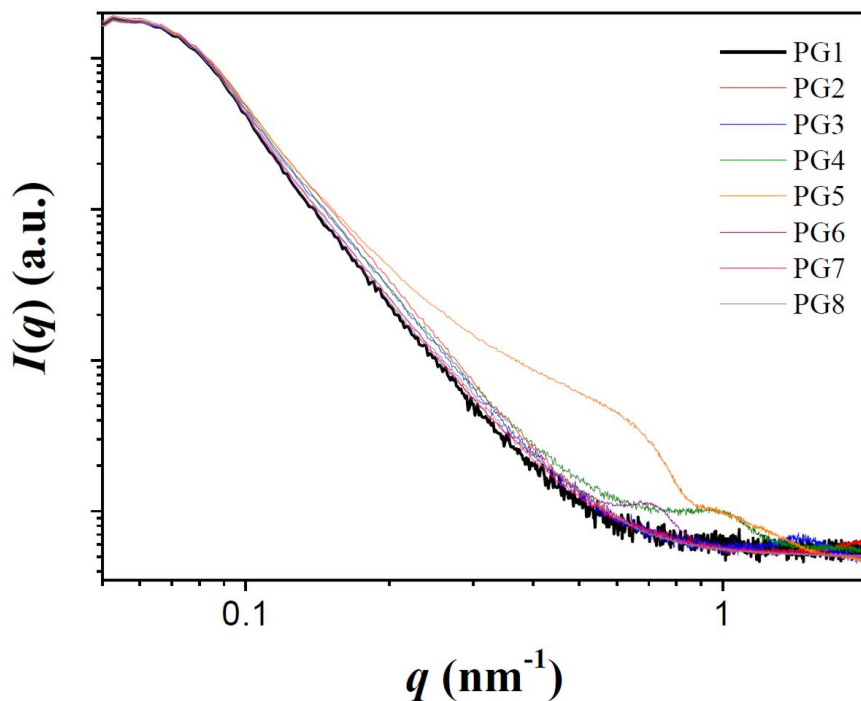


Figure S 21: SAXS curves of freeze-dried DP powders (PG1 – PG8, series A), demonstrating some unaided self-assembly for PG4 – PG6.

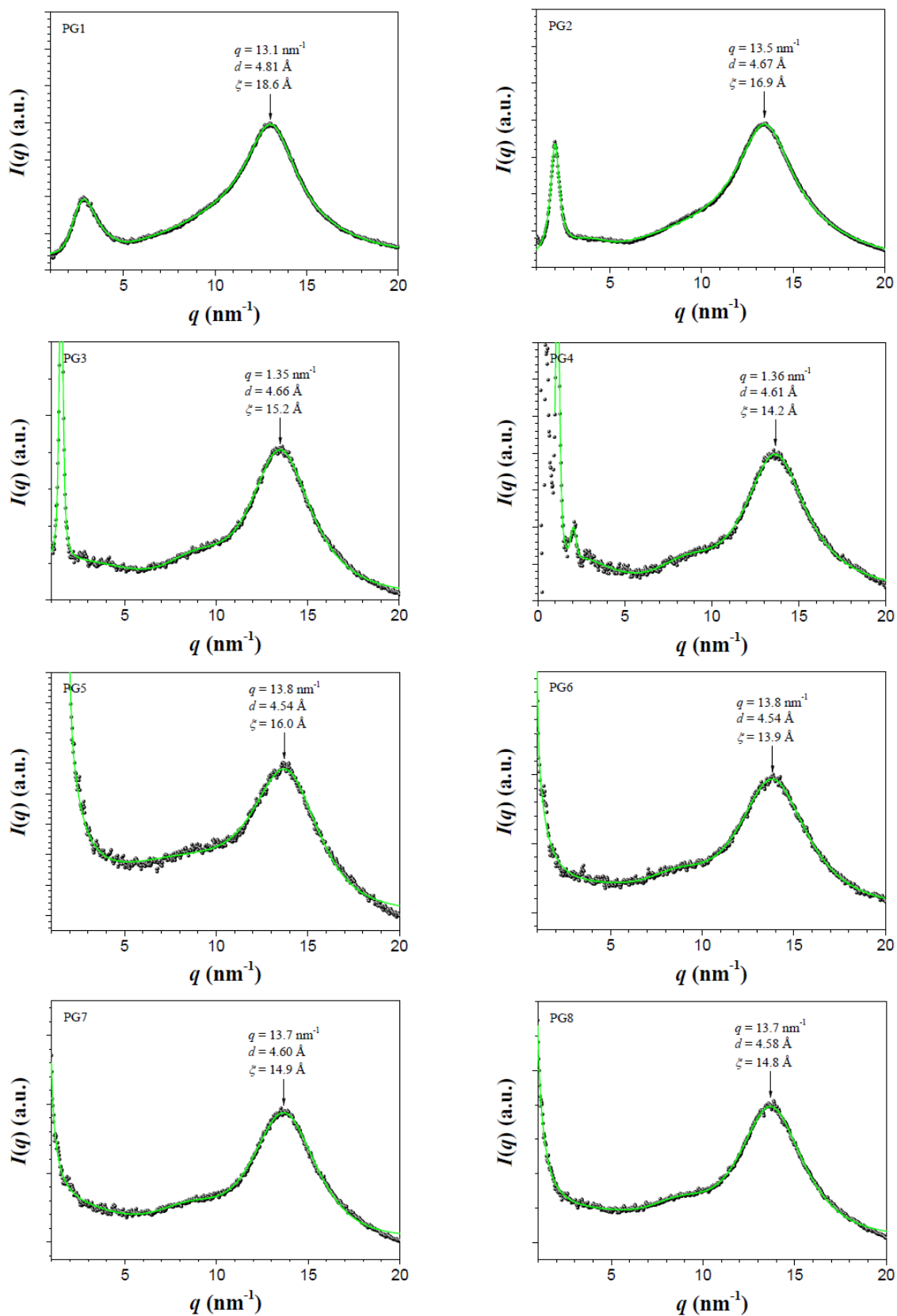


Figure S 22: WAXS curves for annealed DP pills (PG1 – PG8, series A) and corresponding curve fits (green lines)

6. Bibliography

- (1) Zhang, B.; Wepf, R.; Fischer, K.; Schmidt, M.; Besse, S.; Lindner, P.; King, B. T.; Sigel, R.; Schurtenberger, P.; Talmon, Y.; et al. The Largest Synthetic Structure with Molecular Precision: Towards a Molecular Object. *Angew. Chem. Int. Ed.* **2011**, *50* (3), 737–740.
- (2) Yu, H.; Schlüter, A. D.; Zhang, B. Synthesis of High Generation Dendronized Polymers and Quantification of Their Structure Perfection. *Macromolecules* **2014**, *47* (13), 4127–4135.
- (3) Yu, H.; Schlüter, A. D.; Zhang, B. Synthesis of Dendronized Polymers by a “n + 2” Approach. *Macromolecules* **2012**, *45* (21), 8555–8560.
- (4) Messmer, D.; Kröger, M.; Schlüter, A. D. Pushing Synthesis towards the Maximum Generation Range of Dendritic Macromolecules. *Macromolecules* **2018**, *51* (14), 5420–5429.
- (5) Yu, H.; Schlüter, A. D.; Zhang, B. Main-Chain Scission of a Charged Fifth-Generation Dendronized Polymer. *Helv. Chim. Acta* **2012**, *95* (12), 2399–2410.
- (6) Messmer, D.; Bertran, O.; Kissner, R.; Alemán, C.; Schlüter, A. D. Main-Chain Scission of Individual Macromolecules Induced by Solvent Swelling. *Chem. Sci.* **2019**, *10*, 6125–6139.
- (7) Costa, L. I.; Storti, G.; Morbidelli, M.; Zhang, X.; Zhang, B.; Kasëmi, E.; Schlüter, A. D. Kinetics of Free Radical Polymerization of Spacerless Dendronized Macromonomers in Supercritical Carbon Dioxide. *Macromolecules* **2011**, *44* (11), 4038–4048.
- (8) Shu, L.; Gössl, I.; Rabe, J. P.; Schlüter, A. D. Quantitative Aspects of the Dendronization of Dendronized Linear Polystyrenes. *Macromol. Chem. Phys.* **2002**, No. 203, 2540–2550.
- (9) Zhang, B.; Yu, H.; Schlüter, A. D.; Halperin, A.; Kröger, M. Synthetic Regimes Due to Packing Constraints in Dendritic Molecules Confirmed by Labelling Experiments. *Nat. Commun.* **2013**, *4*, 1993.
- (10) Zhang, B.; Wepf, R.; Kröger, M.; Halperin, A.; Schlüter, A. D. Height and Width of Adsorbed Dendronized Polymers: Electron and Atomic Force Microscopy of Homologous Series. *Macromolecules* **2011**, *44* (17), 6785–6792.
- (11) Costanzo, S.; Scherz, L. F.; Schweizer, T.; Kröger, M.; Floudas, G.; Schlüter, A. D.; Vlassopoulos, D. Rheology and Packing of Dendronized Polymers. *Macromolecules* **2016**, *49* (18), 7054–7068.
- (12) Winkler, H. Computerunterstützte Interpretation Elektronenmikroskopischer Bilder von Dekorierten Und Beschatteten Biologischen Oberflächen, ETH Zürich, 1986.
- (13) Sheiko, S. S.; Sumerlin, B. S.; Matyjaszewski, K. Cylindrical Molecular Brushes: Synthesis, Characterization, and Properties. *Prog. Polym. Sci.* **2008**, *33* (7), 759–785.
- (14) Bertran, O.; Zhang, B.; Schlüter, A. D.; Kröger, M.; Alemán, C. Modeling Nanosized Single Molecule Objects: Dendronized Polymers Adsorbed onto Mica. *J. Phys. Chem. C* **2015**, *119* (7), 3746–3753.
- (15) Tacke, S. Sebastian’s QSTEM Paper. *Same as this Pap.* **2019**, Preceding this article in the journal.
- (16) Krzyžánek, V.; Müller, S. A.; Engel, A.; Reichelt, R. MASDET—A Fast and User-Friendly Multiplatform Software for Mass Determination by Dark-Field Electron Microscopy. *J. Struct. Biol.* **2009**, *165* (2), 78–87.
- (17) Bertran, O.; Zhang, B.; Schlüter, A. D.; Halperin, A.; Kröger, M.; Alemán, C.; Spellmeyer, D. C.;

- Fox, T.; Caldwell, J. W.; Kollman, P. A.; et al. Computer Simulation of Dendronized Polymers: Organization and Characterization at the Atomistic Level. *RSC Adv.* **2013**, *3* (1), 126–140.
- (18) Bertran, O.; Zhang, B.; Schlüter, A. D.; Kröger, M.; Alemán, C. Computer Simulation of Fifth Generation Dendronized Polymers: Impact of Charge on Internal Organization. *J. Phys. Chem. B* **2013**, *117* (19), 6007–6017.
- (19) Lee, B.; Lo, C.-T.; Thiyagarajan, P.; Winans, R. E.; Li, X.; Niu, Z.; Wang, Q. Effect of Interfacial Interaction on the Cross-Sectional Morphology of Tobacco Mosaic Virus Using GISAXS. *Langmuir* **2007**, *23* (33), 11157–11163.
- (20) Scherz, L. F.; Costanzo, S.; Huang, Q.; Schlüter, A. D.; Vlassopoulos, D. Dendronized Polymers with Ureidopyrimidinone Groups: An Efficient Strategy To Tailor Intermolecular Interactions, Rheology, and Fracture. *Macromolecules* **2017**, *50* (13), 5176–5187.
- (21) Messmer, D.; Böttcher, C.; Yu, H.; Halperin, A.; Binder, K.; Kröger, M.; Schlüter, A. D. 3D Conformations of Thick Synthetic Polymer Chains Observed by Cryogenic Electron Microscopy. *ACS Nano* **2019**, *13*, 3466–3473.